2024

A Near Field Lagrangian Particle Modeling for the Multiphase Flow of Reaction Control System Thrusters in Space Environments

Janice Zou
University of Central Florida

STARS Citation
Zou, Janice, "A Near Field Lagrangian Particle Modeling for the Multiphase Flow of Reaction Control System Thrusters in Space Environments" (2024). *Graduate Thesis and Dissertation 2023-2024*. 276.
https://stars.library.ucf.edu/etd2023/276

A NEAR FIELD LAGRANGIAN PARTICLE MODELING FOR THE MULTIPHASE FLOW OF REACTION CONTROL SYSTEM THRUSTERS IN SPACE ENVIRONMENTS

by

JANICE ZOU
B.S. University of Central Florida, 2023

A thesis submitted in partial fulfilment of the requirements
for the degree of Master of Science
in the Department of Mechanical and Aerospace Engineering
in the College of Engineering and Computer Science
at the University of Central Florida

Summer Term
2024

Major Professor: Michael P. Kinzel

ABSTRACT

In the current age of space exploration, the push to reach further to deep space presents a greater need for analysis and verification and validation of rocketry components in the space environment. Due to the nature of space, firings of rocket thrusters in space is a multi-regime problem. With the low density, pressure, and temperature of the environment, the resultant plume structure, seeded with unburnt fuel droplets, extends up to multiple orders of magnitude in distance as compared to a plume structure in the Earth's atmosphere. The frozen droplets, or particles, create concerns including surface contamination and erosion, calling a cause for study and model development to understand particle behavior in this multi-regime environment. This work intends to develop a model to analyze and understand multiphase flow and particle behavior in this environment utilizing the lower fidelity, but more computationally efficient, RANS turbulence modeling. Particle properties are compared against a regime-defining parameter to understand the trends in behavior. Finally, the work closes out on a preliminary look into implementing fully reacting flow chemistry for the multiphase flow. These results and progress are promising in developing an efficient model that may be integrated into a hybrid model to better predict particle behavior and dispersion in this multi-regime environment.

To my mom, dad, and friends.

ACKNOWLEDGMENTS

The past year or so has been a whirlwind of things to do and an abundance of learning both on a personal and academic level. I would like to take this time to truly thank Dr. Michael Kinzel and Dr. Jonathan Pitt; it has been a rough journey of learning but I am extremely grateful and honored to have been under their guidance as I would not be here without the opportunities and support through my advisors. I would also like to thank my friends in the Computational Fluids and Aerodnyamics Laboratory at UCF; it has truly been a wonderful year that I am grateful for...all the laughs, late nights, and learning from one another. Thank you all, and here is to our next journey!

TABLE OF CONTENTS

LIST OF FIGURES

LIST OF TABLES

CHAPTER 1: INTRODUCTION

Objective and Motivation

With the inception of the Artemis program, space exploration continues to grow, reaching further into deep space and the universe. More than ever, it has become increasingly important to understand the effects of human-designed space vehicles in space upon their local environment.

When rocket thrusters are fired in space, whether to control its attitude or trajectory, they produce a plume structure that behaves unlike those in the Earth's atmosphere due to the multiple regimes flow experiences. With the low pressure, temperature, and specifically, density of the space environment, fluid particles no longer follow the typical continuum regime behaviors that are governed by a relatively small mean free path up to a Knudsen number of 0.01. This continuum assumption "breaks down" to free molecular (rarefied) flow, governed by relatively larger mean free paths, where the plume structure is capable of expanding to some maximum spreading [1].

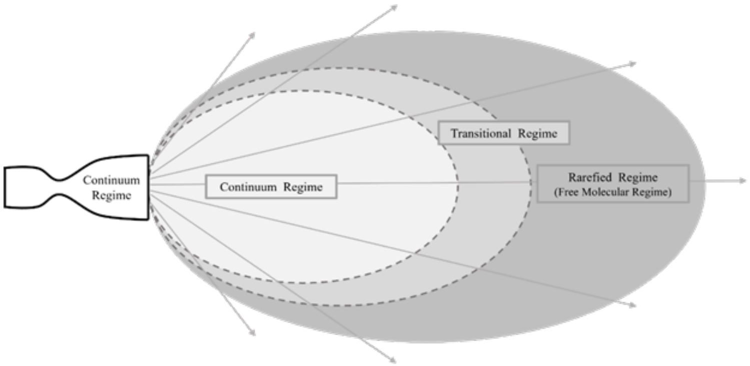

Figure 1.1: Flow Regimes for a Plume in Vacuum Environment

Furthermore, due to the incomplete combustion processes of thruster firings and low temperatures of the environment, unburnt and partially burnt fuel continue traveling such lengths at high velocities [2], [3]. These fuel droplets, or particles, become a concern due to their potential to contaminate optically sensitive surfaces (e.g. cameras, solar arrays) and erode any nearby surfaces of space vehicles [3]–[5], reducing the lifetime of crucial surfaces and/or necessitating costly repairs.

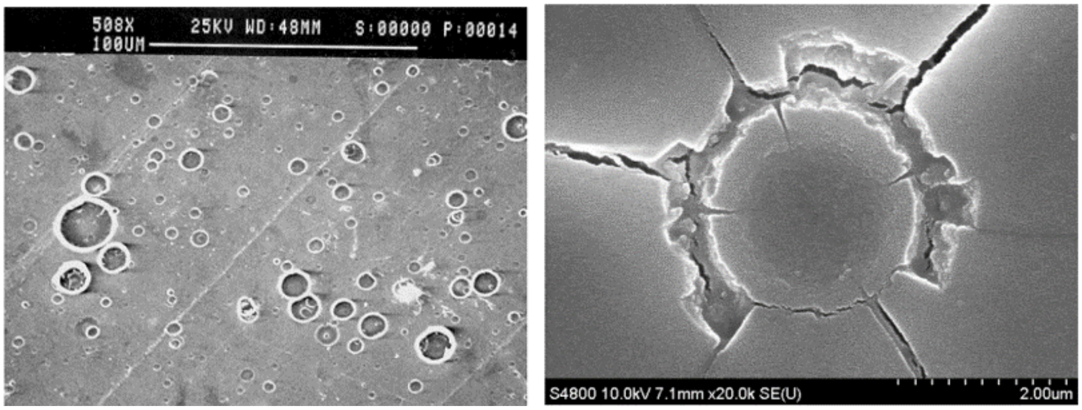

Figure 1.2: Thruster Plume-Induced Droplet Impact Craters at the Microscale

Since the 1900's, liquid propulsion rocket engines (LPREs) have been the most reliable means of propulsion for both military aircrafts and space vehicles (e.g. rockets) due to their high specific impulse, the variety of produced thrust, and their ability for "quick restarts, fast pulsing, and ready reuse" [6]. Most importantly, a LPRE's ability to handle attitude, trajectory, and velocity changes sensitively have made it the ideal method to utilize in many space vehicles since slight alterations produce a large effect in the vacuum environment.

For this work, the focus is on a hypergolic bipropellant rocket engine because of its popular use in space propulsion for attitude and trajectory control. The thruster geometry and specifications of interest are pulled from one of Aerojet Rocketdyne's bipropellant engines: the R-4D-11 490 N thruster [7]. The fuel type utilized in this thruster is the common liquid bipropellant, monomethylhydrazine and nitrogen tetroxide (MMH/NTO; CH_6N_2 and N_2O_4).

Overview of Study

The present work aims to develop and analyze a computational fluid dynamics (CFD) model to understand multiphase flow and particle behavior in the continuum portion of the multi-regime environment experienced when a reaction control system (RCS) thruster is fired in space. Through examining particle properties and dispersion at these regimes, one is better able to understand the effects of a rarefied environment to a flow field. Eventually, data from this CFD model may be integrated into hybrid models utilizing codes to better model the rarefied environment and thus better predict particle behavior and dispersion.

CHAPTER 2: LITERATURE REVIEW

Primer to Computational Fluid Dynamics

For complex fluid flow scenarios, as is of interest in this work with rocket firings in space environments, CFD becomes a strong tool for use in design, analysis, and verification. Traditional methodologies such as experimental and theoretical, or analytical, have been the tools of use in fluid mechanics and heat transfer problems for years, yet with the developments of technology since the inception of the computer in the 19th century, numerical (or computational) methods has grown to become one of the main tools in tandem with experimental and theoretical methods for use in thermofluids work. This is due to the coupling of this growth and the cost of running numerical methods via computers decreasing over the years, even well into the 21st century.

When taking a zooming into the 21st century, the rates and speeds of integer and floating point computations by central processing units (CPUs) have continued to decrease—only near the 2020’s has there been a lesser degree of decline paired with a slight increase due to physical limitations of CPU designs now being the main barrier [6].

There are various methodologies of CFD, which include the traditional methods of finite difference, finite volume, and finite element. The finite volume (FV) method is the most common and will thus be the foundation for discussion. For a control volume of interest, FV subdivides the entire control volume into subsequent smaller volumes where data from one small volume interacts and exchanges information with its surrounding neighbors; with this, the governing Navier-Stokes equations are therefore written and solved as integrals. Note that the Navier-Stokes equations are non-linear and thus values of properties are solved iteratively—such as by the Jacobi method, Gauss-Seidel method, or successive overrelaxation (SOR), with some criterion for convergence of the iterated values. A further discussion of the governing equations is found in the Methodology section.

Ground Experiments in Relation to Plume Studies

Effects of thruster plumes firing in space had been of great concern with every advancement of space exploration, but especially so with the development of the International Space Station (ISS) in the early 21st century. Adverse effects—specifically contamination—were studied beginning with ground-based experiments as those developed and published, such as the standardized hot test firings of small bipropellant and monopropellant thrusters in vacuum chambers by Trinks [2] and the propulsion system tests by Ivanov et. al [7]. In Trinks' experiments, transient thruster firing data such as thrust and force, impulse, heat, and droplet outflows were collected and analyzed for the specific bipropellant and monopropellant thrusters of their interest. Droplet angular distribution for one of the bipropellant nozzles were also recorded. The experiment by Ivanov et. al provides observed parameters for a small cold flow thruster, specifically density distribution along the nozzle exit plane, temperatures along the centerline with respect to a continuum breakdown parameter, and relative pressure.

Although the different bipropellant and monopropellant engines studied by Trinks had resulted in different values of such parameters (i.e. thrust, impulse, heat, droplet outflows), a general relationship can be discerned between transient thrust and force graphs to droplet outflow and dispersion graphs for a 66 N bipropellant nozzle. The properties measured in Figure 2.1 show evidence that upon initial firing, as well as with the completion of the firing pulse (or tail-off [1]), an abundance of these particles were found being ejected from the bipropellant nozzles. It is important to note that while these engines are running at steady state, the phase in between start-up and tail-off, the presence of these fuel particles being exhausted from the nozzle are significantly less.

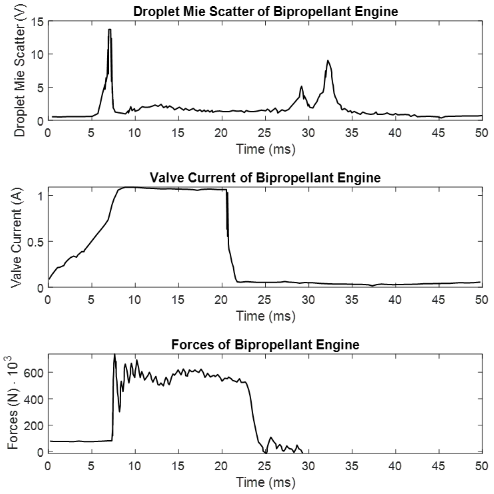

Figure 2.1: Droplet Presence During Firing of Thruster

Such information by Trinks provides extremely meaningful validation data for the development of a simulated transient rocket thruster hot firing. The replication of this transient experiment as a CFD simulation, where particle presence mimics that as captured in the mie scatter, is the goal that this study and future work will ultimately build up to.

Numerical Models and Flight Experiments for Plume Studies

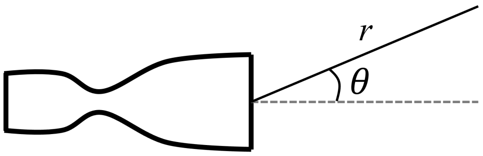

Figure 2.2: Axisymmetric Coordinates of Thrusters

To define the behaviors seen by the ground experiments, numerical models were proposed by engineers, including Larin, at the National Aeronautics and Space Administration (NASA)

Johnson Space Center [3]. RCS nozzles may typically be considered to be axisymmetric, where the axis is taken at the centerline of the nozzle. For axisymmetric nozzles defined by the polar coordinates system shown in Figure 2.2, droplet number flux distribution, (Equation 2.1), and droplet velocities, (Equation 2.2), were defined.

$$\dot{n}(T,d,r,\theta) = \frac{\dot{M}_T \cdot KT^{-\beta}}{S_m} \cdot (r + l_{noz})^{-2} \cdot (\frac{d}{d_{min}})^{-p} \cdot e^{\frac{\theta^2}{2\sigma^2}} \tag{2.1}$$

$$V(T,d,\theta) = \left[0.7e^{-0.015\left(\frac{d}{d_{min}}\right)^{1.19}} + 0.3\right] \cdot \left[0.0277 \cdot ln\left(\frac{T}{T_{min}}\right) + 0.6811\right] \cdot U_{lim} \tag{2.2}$$

In the development of these models, it is important to note that the authors made the following assumptions, and thus when utilizing the models these must be considered during analysis:

1. Plume droplets develop in the combustion chamber but are then blown out by the exhaust; particles attached to the nozzle walls (from previous firings' deposition) are ignored.
2. Plume droplets do not interact with one another; all secondary breakup, evaporation, freezing, and effects on gas flow parameters are ignored.
3. Droplets are liquid and perfect spheres.
4. Beyond a defined limiting angle, there are no droplets of a specific size in the plume.
5. Droplet size distribution based on the plume axis does not vary between different thrusters.

As such and by specifically defining the droplets in a discrete manner, it is evident that a Eulerian-Lagrangian methodology is developed by the authors, where the gaseous exhaust is modeled in a Eulerian perspective with Lagrangian particles to act as the unburnt fuel particles.

Previous work in explicitly studying contamination in true space have been completed by researchers at NASA, serving as validation of the ground experiments' results in the low-pressure, low-density, and low-temperature environment. The two main experiments which measured and characterized contamination were the Shuttle Plume Impingement Flight Experiment (SPIFEX) and the Plume Impingement Contamination (PIC) flight experiment [4]. Results from these experimentation present ways in which plumes in space may cause concerns: contamination deposition upon surfaces and erosion of surfaces by high-speed impacts from the droplets of the plume. These experiments also show that depending on the material, chemical reactions between the fuel particle and the impacted surface may be an additional cause to the degradation. Reported data from SPIFEX state that for an aluminum sample, impacts were scanned to be 740 impacts/mm^2, while a Kapton (reactive material to the fuel) sample measured 2,200 impacts/mm^2. These samples were placed from 8 to 76 feet away from the firing engines, allowing for the capturing of data near and far from the nozzle exit plane. Note that by defining the measurements at such a small scale, despite the micrometer size of these particle impact craters, the density of impacts is significant enough to cause concern at the macroscopic scale of space vehicles when considering the lifetime of parts as well as the overall missions.

The previous numerical models proposed by Larin et. al, based off experiments by Trinks, were expanded upon and further improved by Soares et. al [5]. Previous parameters of maximum droplet diameter, d_{max}, and droplet size distribution parameter, p, were refined to better reflect the image analysis of the impacted SPIFEX sample materials—d_{max} of interest decreased from 100µm to 12µm and droplet distribution decreased from 4.57 to 1.7. The remaining parameters are similarly defined in both instances. Soares et. al implemented a software to further identify craters from the particle impacts from the experiments; it is to note that although there were some "potential" pits identified that may or may not have resulted from plume impingement, even by neglecting them, there was no change to the overall percentage of area affected by the plume particle impacts. The issue of surface erosion and cratering found upon surfaces thus mainly stems from the high-speed impacts of these exhausted plume particles. Being able to accurately model and understand the behaviors of these particles proves to be a critical step in ensuring the use of RCS thrusters while considering the functionality of components and surfaces nearby.

Previous Methodologies in Modeling Thruster Plumes

In developing a better analysis of plume particle dispersion and impingement in space, one may look to previous methodologies and simulations of similar work. Lumpkin and Larin from NASA Johnson Space Center concentrated on the development and analysis of the firing of multiple R-4D thrusters in space, handling both the continuum and rarefied flow regimes [8] in a hybridized manner. Similarly, Lee analyzed both reactive mono- and bipropellant rocket thrusters, coupling models to handle both continuum and rarefied flow regimes [9], [10]. Later on, Hou, Fu, and Ba developed an axisymmetric model of a classical bipropellant monomethylhydrazine/nitrogen tetroxide (MMH/NTO) rocket engine, focusing on the inflow conditions with the implementation of a simplified chemical reaction scheme [11].

Lumpkin and Larin's physical model included an axisymmetric nozzle geometry with an arbitrary external flow domain to capture plume formation in the continuum regime and the breakdown of the flow. Lee's continuum domain consists of the nozzle, which feeds as an inflow parameter to the rarefied regime calculations at the nozzle exit plane. Hou, Fu, and Ba's physical model was of an axisymmetric nozzle, including an extended upstream region for its combustion chamber. All instances have specified outlets with vacuum conditions to mimic the space environment.

The axisymmetric continuum flow models of the mentioned works implemented reaction schemes of the common MMH/NTO propellant in a turbulent flow, however the specifics of the reaction process for each scheme varied. Lumpkin and Larin utilized an 11-species 86-reaction gas flow and disabled reactions to mimic chemically frozen flow approximately halfway in the diverging section of the nozzle; this was a feasible assumption for the model due to the drastic drop in gas temperature for the space environment specified. It was also noted that viscous terms were disabled just downstream of the nozzle exit plane due to the rarefication of flow and the domination of the convective terms of the Navier-Stokes equations. Lee specifies a global chemical equilibrium reaction for gaseous MMH/NTO where 11 elementary equilibrium equations are solved simultane-

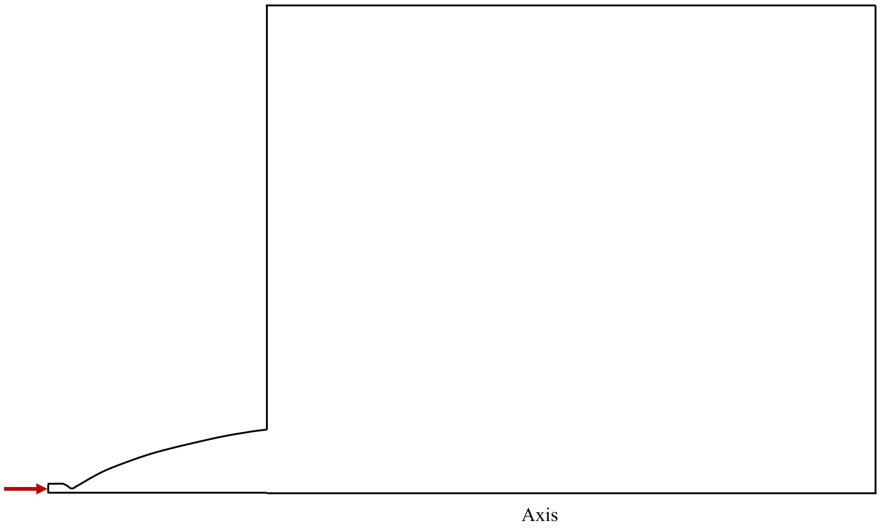

(a) Lumpkin and Larin [8]

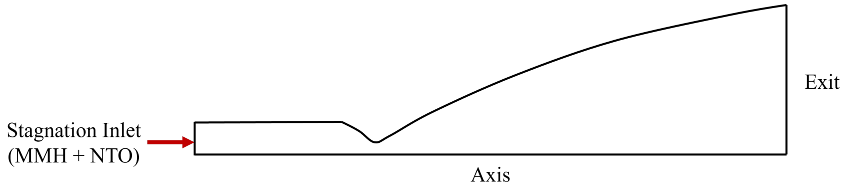

(b) Lee [9], [10]

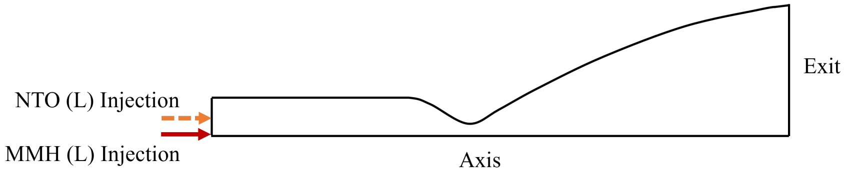

(c) Hou, Fu, and Ba [11]

Figure 2.3: Sketch of Continuum Domains Defined for Previous Works in Literature

ously for the equilibrium constants. Following this process, moles of the gaseous species, entropy, heat of reaction , and other thermodynamic properties are calculated for the final stagnation conditions for use as the inflow condition. On the other hand, Hou, Fu, and Ba utilized a 23-species 20-reaction with active chemistry through the entire nozzle geometry. This simulation specified the injection of MMH/NTO as swirling liquid sprays that were quickly evaporated in the chamber to give way to the gaseous forms of which were mixed and reacted. The mixture of the fuel was considered uniform with no regard for fluid mixing, and the rate of conversion was only dependent on reaction rates. Unlike the method described in Lumpkin and Larin's work, both inviscid and viscous terms of the flow equation were solved.

CHAPTER 3: METHODOLOGY

Governing Equations

When discussing the representation and analysis of fluid dynamics, specifically in using computational methods, the fundamental governing equations of fluid dynamics are imperative for definition. Conservation of mass, conservation of momentum, and conservation of energy define the physics of fluids for this problem of interest. In the reality of turbulent, chemically active flow for a firing rocket engine in space, where pressure, temperature, and density are low, there are several simplifications taken to the analysis. The “fluid” of space is considered to be a compressible, low-density gas that is non-reactive to the firing nozzle flow—in this work, a “ghost species” of helium acts as the ”fluid” of space. Both the ghost specie and the flow from the nozzle are treated as a calorically perfect, ideal gas which may be defined by Equation 3.1 because molecules in a space (low density) environment have a larger mean free path—molecules, as seen in Figure 3.1, are further apart and experience little to no intermolecular forces [12]. The fluid is also approximated to be isentropic through the nozzle as the flow is adiabatic and flow properties do not experience an extremely rapid change [1].

$$pV = MR_0T \tag{3.1}$$

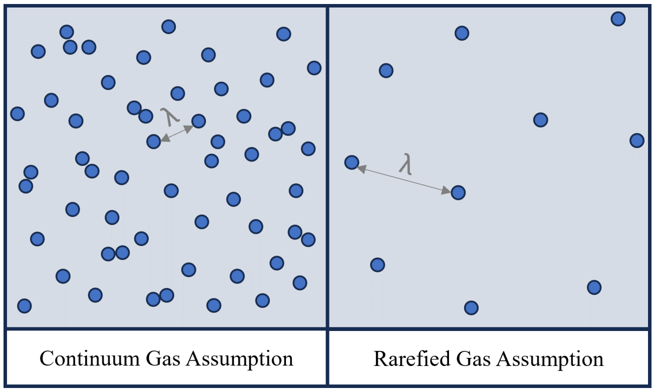

Figure 3.1: Continuum Assumption vs Rarefied Assumption

In implementation of the governing equations to the context of the real flow scenario, the general equations are modified to incorporate turbulence and a source term, S_u, which may include a chemical source term to consider the prevalent species and reactions of the flow. Mindful to the computational cost of this work, the Reynolds-Averaged Navier-Stokes (RANS) equations are used to define the flow and solved. A selected eddy viscosity turbulence model, $k-\omega$, is fully incorporated to the transport phenomenon to close the RANS equations (momentum); more on the specific two-equation model will be discussed later. Note that in the utilized commercial code for this work, the added chemical source term from the reacting flow process is originally internally calculated but may be user-defined. With the intentions of this work, the source term calculation remains at its default. Thus, conservation of mass, momentum, and energy are defined as follows:

$$\frac{\partial}{\partial t}\int_V \rho \, dV + \oint_A \rho v \cdot dA = \int_V S_u \, dV \tag{3.2}$$

$$\frac{\partial}{\partial t}\int_V \rho \, dV + \oint_A \rho v \otimes v \cdot dA = -\oint_A pI \cdot dA + \oint_A T \cdot dA + \int_V f_b \, dV + \int_V S_u \, dV \tag{3.3}$$

$$\frac{\partial}{\partial}\int_V \rho E \, dV + \oint_A \rho H v \cdot dA = -\oint_A \dot{q} \cdot dA + \oint_A T \cdot v \cdot dA + \int_V f_b \, dV + \int_V S_u \, dV \tag{3.4}$$

Simcenter STAR-CCM+ (18.02.008), a commercial CFD solver developed by Siemens Digital Industries Software, is the code that this work builds from. STAR-CCM+ utilizes a finite volume discretization upon the control volume specified. These volume-discretized equations are solved in a coupled manner, whereby velocity is found through the momentum equations, while pressure and density may be derived from the continuity equation.

For the context of analyzing plume particles in the flow, it is important to be able to consider both near-wall interactions and free-stream interactions. To close the turbulent kinetic energy equation, k, and the moments of the RANS equations, the two-equation $k - \omega$ turbulence model shown below is utilized.

$$\frac{\partial}{\partial t}\rho k + u_i \frac{\partial}{\partial t}\rho k = \tau_{ij}\frac{\partial u_i}{\partial x_j} - \beta^* \rho \omega k + \frac{\partial}{\partial x_j}\left[(\mu + \sigma_{k2}\mu_t)\frac{\partial k}{\partial x_j}\right] \tag{3.5}$$

$$\frac{\partial}{\partial t}\rho \omega + u_i \frac{\partial}{\partial t}\rho \omega = \frac{\gamma_2}{v_t}\tau_{ij}\frac{\partial u_i}{\partial x_j} - \beta \rho \omega^2 + \frac{\partial}{\partial x_j}\left[(\mu + \sigma_{\omega}\mu_t)\frac{\partial \omega}{\partial x_j}\right] \tag{3.6}$$

More specifically, STAR-CCM+'s modified $k - \omega$ SST model is applied because of its ability to capture near-wall shear flow while maintaining the capabilities and strengths of the $k - \epsilon$ model's shear flow prediction further in the free-stream with implementation of the cross-diffusion term through a blending function [13], [14].

Eulerian-Lagrangian Method

This work is partitioned into two sections both of which utilize a Eulerian-Lagrangian approach to develop a transient particle tracking model:

1. MMH/NTO gaseous products at chemical equilibrium with liquid MMH and liquid NTO particles (cold flow nozzle and extended domain);
2. MMH/NTO injection with chemical reactions (reacting chemistry nozzle).

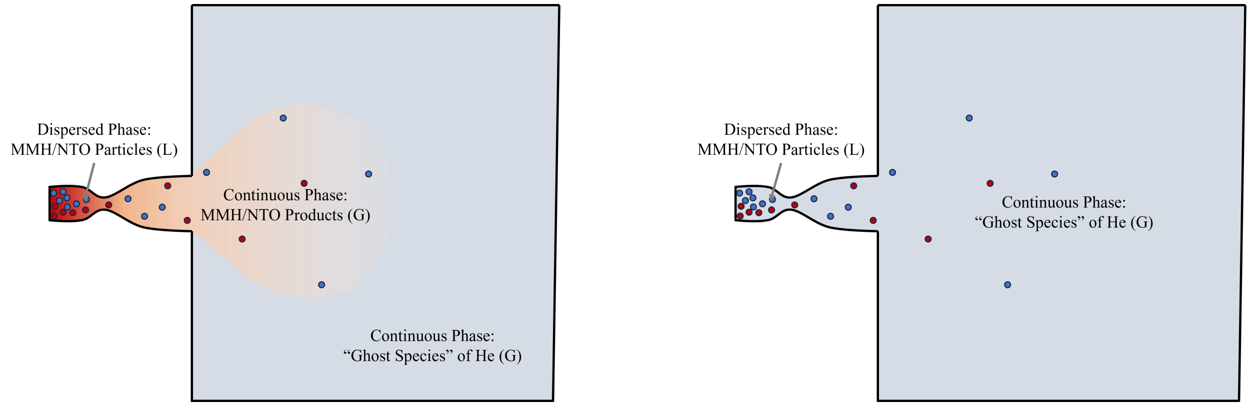

(a) Gaseous Products and MMH/NTO Liquid Particles at Chemical Equilibrium

(b) MMH/NTO Liquid Particles with Reactions

Figure 3.2: Continuous versus Dispersed Phases of Study

For these models, the “ghost species” is a continuous phase of the fluid that is initialized throughout the entire flow domain, including within the nozzle geometry. In the cold flow, the gaseous products at chemical equilibrium are defined at the inlet and act as the continuous phase of the rocket firing; the liquid MMH and NTO particles which define the dispersed phase are similarly included at the nozzle. Note that in this present study, the second method is simplified to a gaseous reacting injection for the nozzle rather than the liquid reacting injection that is observed in reality.

The continuous and dispersed phase for this model is two-way coupled, whereby properties of the particles affect the bulk flow while the bulk flow also affects the particles. Mass is transferred from each of the particles found in a computational cell to the continuous phase of the fluid, resulting in a source term that defines the summed rate of mass transfer from the particles, S_m. Similarly, the momentum of each of the particles are also transferred at some rate to the continuous phase with the source term S_v. The energy equation is also altered with a source term, S_E, accounting for the rate of the total energy transferred from the particles in a cell to the continuous phase.

$$S_m = -\frac{1}{\Delta t} \sum_{\pi} \left(\int_{t}^{t+\Delta t} \int_{V_c} \delta(r - r_\pi) n_\pi \dot{m} \, dV \, dt \right) \tag{3.7}$$

$$S_v = -\frac{1}{\Delta t} \sum_{\pi} \left(\int_{t}^{t+\Delta t} \int_{V_c} \delta(r - r_\pi) n_\pi (F_s + \dot{m} v_p) \, dV \, dt \right) \tag{3.8}$$

$$S_E = -\frac{1}{\Delta t} \sum_{\pi} \left(\int_{t}^{t+\Delta t} \int_{V_c} \delta(r - r_\pi) n_\pi (Q_t + F_s \cdot v_p + \frac{1}{2} \dot{m}_p v_p^2 + \dot{m}_p h) \, dV \, dt \right) \tag{3.9}$$

In both instances of the approach, the Lagrangian Multiphase model of STAR-CCM+ plays a critical role in implementing tracking of plume particles for the multiphase flow scenario. This model redefines the conservation equations for each of the phases involved. For the dispersed phase, the equations are rewritten in Lagrangian form as a means to define each of the particles and their motion; the conservation of linear and angular momentum for the particles may be defined by **??** and **??**, where F_s and F_b are the resultant surface and body forces while M_b and M_c are the moments due to rotational drag and total moment from any contact forces. The continuous phase is laid out in Eulerian form with a modification in consideration of the existence of the particles (i.e. addition of the source terms S_m, S_v, and S_E).

$$m_p \frac{d\mathbf{v}_{\boldsymbol{p}}}{dt} = \boldsymbol{F_s} + \boldsymbol{F_b} \tag{3.10}$$

$$\mathbf{I}_{\boldsymbol{p}} \frac{d\boldsymbol{\omega_p}}{dt} = \boldsymbol{M_b} + \boldsymbol{M_c} \tag{3.11}$$

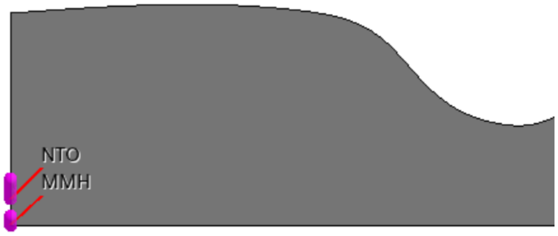

Figure 3.3: Injection Definition for Liquid Particles

Injectors are implemented into the STAR-CCM+ model to mimic the Lagrangian particles of interest: the unburnt MMH/NTO droplets exhausted from the nozzle. Placed along the inlet boundary as shown in Figure 3.3 with 20 points per injector to roughly mimic fuel injection in the real world, the MMH and NTO droplets were given the following diameters, velocities, and directions.

Table 3.1: Definitions for MMH/NTO Particles

Particle Material	Particle Diameter [m]	Particle Velocity [m/s]	Particle Direction (x, y)
Monomethylhydrazine (MMH)	3.40 E-05	25.42	(0.707, 0.707)
Nitrogen Tetroxide (NTO)	2.50 E-05	20.18	(0.574, 0.819)

Defining the Flow and Particles

In defining the flow regimes experienced when firing in space, one of the common parameters utilized to differentiate the flows may be Knudsen number, Kn: a non-dimensional value which measures a ratio of the mean free path of molecules to a characteristic length which defines the flow problem. Observing a global Knudsen number, defined through the overall flow, the mean free path will consider d, the diameter of the liquid particles, and the temperature and pressure of the continuous phase. The characteristic length of interest for analysis is taken to be the radius of the exit plane for the entire flow domain. When analyzing the particles specifically, the characteristic length of interest is taken to be the respective diameter of the particles.

$$Kn_{global} = \frac{\lambda}{L_c} \tag{3.12}$$

where the mean free path, λ, is defined by

$$\lambda = \frac{kT_{gas}}{\sqrt{2}\pi \bar{d}_{gas}^{2} p_{gas}} \tag{3.13}$$

where k is Boltzmann's constant, T_{gas} and p_{gas} are the temperature and static pressure of the gas, and d_{gas} is the mean diameter of the gaseous molecule.

Due to these two differing phases and the nature of the multi-regime problem, properties of the particles are defined specifically. The particle Reynolds number is calculated as in Equation 3.14, where the subscript p signifies the particle's property, the subscript g represents the bulk gas and/or fluid characteristic, and $\boldsymbol{\omega}$ is the velocity of the particle relative to the bulk fluid [15].

$$Re_p = \frac{\rho_g \left|\boldsymbol{\omega}\right| d}{\mu_g} \tag{3.14}$$

Similarly, the particle drag is also defined while considering the differing regimes that may be experienced by the particle throughout its trajectory. Recalling the assumptions for particles in the numerical model by Larin et. al and Soares et. al, the droplets in these models will be considered spheres. At supersonic speeds, as is seen by RCS thruster flows, and with the multiple regimes present in a firing event in space, drag on a particle is no longer accurately accounted for by the original Schiller-Neumann drag coefficient definition for spherical liquid droplets. In their model, Larin et. al modify the empirical relations for continuum flow with the addition of a rarefaction coefficient, C_{Kn}.

$$C_D = \begin{cases} \frac{24}{Re} \cdot (1 + 0.15 \cdot Re^{0.687}) \cdot C_{Kn}, & Re < 1000 \\ 0.424 \cdot C_{Kn}, & Re > 1000 \end{cases} \tag{3.15}$$

More recently, Loth et. al developed a modified drag equation which accounts for high speeds in the compressible continuum regime, the rarefied regime, and the behavior between the two. In the continuum regime, C_D is defined as:

$$C_D = \frac{24}{Re_p}\left(1 + 0.15 Re_p^{0.687}\right) H_M + \frac{0.42 C_M}{1 + \left(\frac{4200}{Re_p^{1.16 C_M}}\right) + \left(\frac{C_M}{Re_p^{0.5}}\right)} \tag{3.16}$$

where

$$C_M = \begin{cases} 1.65 + 0.65\tanh(4Ma_p - 3.4), & Ma_p < 1.5 \\ 2.18 - 0.13\tanh(0.9Ma_p - 2.7), & Ma_p > 1.5 \end{cases} \tag{3.17}$$

$$G_M = \begin{cases} 166Ma_p^3 + 3.29Ma_p^2 - 10.9Ma_p + 20, & Ma_p < 0.8 \\ 5 + 40Ma_p^3, & Ma_p > 0.8 \end{cases} \tag{3.18}$$

$$H_M = \begin{cases} 0.0239Ma_p^3 + 0.212Ma_p^2 - 0.074Ma_p + 1, & Ma_p < 1 \\ 0.93 + \frac{1}{3.5 + Ma_p^5}, & Ma_p > 1 \end{cases} \tag{3.19}$$

In the event the flow field's density is reduced and the particles experience conditions likened to a rarefied flow regime, Loth et. al defines drag for this environment where Kn_p are finite and Re_p is less than 45 [15]. Note the difference in the defining particle Reynolds number for the classification of the flow regime drag between Larin et. al's model (Re_p = 1,000) and Loth et. al's model (Re_p = 45).

$$C_D = \frac{C_{D,fm}}{1 + \left[\left(\frac{C_{D,fm}}{J_M}\right) - 1\right]\sqrt{\frac{Re_p}{45}}} \tag{3.20}$$

where

$$C_{D,fm} = \frac{(1+2s^2)exp(-s^2)}{s^3\sqrt{\pi}} + \frac{(4s^4+4s^2-1)\text{erf}(s)}{2s^4} + \frac{2}{3s}\sqrt{\pi} \tag{3.21}$$

$$s = M_p\sqrt{\frac{\gamma}{2}} \tag{3.22}$$

$$f_{Kn} = \frac{1}{1 + Kn_p\left[2.514 + 0.8\text{exp}\left(\frac{-0.55}{Kn_p}\right)\right]} \tag{3.23}$$

In such, note that s, the molecular speed ratio, is dependent on the Mach number of the particle and the specific heat ratio of the gas. f_{Kn}, the Cunningham correction factor is defined to address and consider the Knudsen number of the particle when equal to one or much less than one [15].

Reacting Chemistry

When implementing active reactions and chemistry, the conservation of mass and momentum defined earlier are solved as usual, however the energy equation is rewritten as a means to account for heat flux from the reaction process. From Equation 3.4, energy is rewritten as follows with the source term that also account for the reactions:

$$\frac{\partial}{\partial t}\int_V \rho E\,dV + \oint_A \rho H\mathbf{v}\cdot\,d\mathbf{a} = -\oint_A \mathbf{q"}\cdot\,d\mathbf{a} + \oint_A \mathbf{T}\cdot\mathbf{v}\cdot\,d\mathbf{a} + \int_V S_E\,dV \tag{3.24}$$

As the governing equations for flow are solved, so are those which conserve the species that are within the reactions:

$$\frac{\partial}{\partial t}\int_V \rho E\, dV + \oint_A \rho H \mathbf{v} \cdot d\mathbf{a} = -\oint \left[J_i + \frac{\mu_i}{\sigma_t} \nabla Y_i \right] \cdot d\mathbf{a} + \int_V S_{Y_i}\, dV \tag{3.25}$$

where Y_i refers to the mass fractions of each of the species, J_i is the diffusive flux, and S_{Y_i} is the source term defining the mass fractions produced from the reactions.

For the purposes of implementing a chemically active turbulent flow, a reacting species transport was implemented with use of the Eddy Dissipation Concept model of STAR-CCM+. With the fuel of interest, MMH/NTO, the mixture of the two cause a four-step reaction process of cold flow, high-temperature pyrolysis, hypergolic ignition, and high-temperature combustion [11]. In a short span of two milliseconds (2 ms), this process results in a drastic temperature increase from a room temperature of 298.15 K, to combustion around 3,000 K; during this process, the presence of certain combustion products also drastically increase. Hou, Fu, and Ba found the majority of the species present after combustion include HONO, OH, and H_2O, where the two former see a sharp rise of mole fraction during stage two of the process before dropping quickly; H_2O, the largest amount, continues to be present at a relatively significant fraction of approximately 0.35 through the remainder of the observed process. It should be noted that the two fuels are highly reactive, auto-igniting upon contact and mixing, thus combustion should occur at the ”cold flow” conditions in room temperature.

The combustion of the fuel itself contains a multitude of reactions with many intermediate processes and there is not one exact mechanism implemented for all scenarios of reacting MMH/NTO in existing work. Hou et. al reduces the complexity of the reaction mechanisms for MMH/NTO, leaving only 23 species and 20 reactions to be solved. The mechanism, including the relevant Arrhenius coefficients, temperature exponent, and activation energy are listed below in Table 3.2.

Table 3.2: Simplified Reactions of MMH/NTO

	Reaction	**Arrhenius Coefficient, *A***	**Temperature Exponent, *n***	**Activation Energy, *E* [cal/mol]**
1	$N_2O_4 + M \rightarrow NO_2 + NO_2 + M$	1.96 E+28	-3.80	12849.00
2	$CH_3NHNH_2 + NO_2 \rightarrow CH_3NNH_2 + HONO$	2.20 E+11	0.00	6700.00
3	$CH_3NNH_2 + NO_2 \rightarrow CH_3NNH + HONO$	1.00 E+08	2.00	0.00
4	$CH_3NNH + NO_2 \rightarrow CH_3N_2 + HONO$	2.20 E+11	0.00	6700.00
5	$CH_3NHNH_2 \rightarrow CH_3NNH + H_2$	3.26 E+13	0.00	18700.00
6	$HONO + M \rightarrow NO + OH + M$	8.40 E+12	0.00	17000.00
7	$NO_2 \rightarrow NO + O$	0.76 E+19	-1.27	73290.00
8	$NO_2 + H \rightarrow NO + OH$	0.35 E+15	0.00	1500.00
9	$CH_3N_2 \rightarrow CH_3 + N_2$	3.00 E+06	0.00	0.00
10	$H_2 + OH \rightarrow H_2O + H$	2.16 E+10	1.51	0.00
11	$CH_3 + O \rightarrow H + CH_2O$	8.43 E+13	0.00	0.00
12	$CH_2O + O \rightarrow OH + HCO$	3.90 E+13	0.00	3540.00
13	$HCO + O \rightarrow H + CO_2$	3.00 E+13	0.00	0.00
14	$CH_3 + NO \rightarrow HCN + H_2O$	9.60 E+13	0.00	28800.00
15	$HCN + M \rightarrow H + CN + M$	1.04 E+29	-3.30	126600.00
16	$CN + H_2 \rightarrow HCN + H$	2.10 E+13	0.00	4710.00
17	$NH_2 + H \rightarrow NH + H_2$	4.00 E+13	0.00	3650.00
18	$NH + NO \rightarrow N_2 + OH$	2.16 E+13	-0.23	0.00
19	$H_2 + O \rightarrow H + OH$	5.06 E+04	2.67	6290.63
20	$HCN + OH \rightarrow NH_2 + CO$	1.60 E+02	2.56	9000.00

The simplified mechanism, when compared to other more complex chemical kinetics, shows good agreements with equilibrium temperature reached and ignition time delay [11]; thus, there is good support into the utilization of these reactions for the STAR-CCM+ plume model at hand. The gas thermodynamic data for each of the 23 species of the mechanism were found from Sandia National Laboratories' Chemkin Thermodynamic Data Base [16] and the Argonne National Laboratories' Ideal Gas and Condensed Gas Phase Database for Combustion [17]. There were two approaches in gathering the species required; in the first, the aim was to select species defined at a low temperature of 300 K and high-temperature of 5,000 K to consider for the room temperature (298.15 K) reaction process. It is important to note that by merging various data sources together, two species were not defined at a 300 K low, but rather a 200 K low and a 100 K low. In the second approach, all species properties defined at a low temperature of 200 K and a high-temperature of 6,000 K was selected; with a lower temperature specified, the room temperature at which the reactions would start, would hopefully be captured. The specific reactions files utilized are provided in the Appendix. As it is not within the scope of this work, for a more detailed view of the mechanism's functionality as compared to other mechanisms and kinetics, please refer to the Hou et. al publication.

For the liquid state of the fuels, thermodynamic properties for MMH and NTO were collected from the National Institute of Standards and Technology [18], [19]. The values collected are defined below; note that certain values of liquid MMH could not be defined, specifically standard state pressure, thus the values of NTO were utilized for the study.

Table 3.3: Properties of Liquid MMH and Liquid NTO

Properties	**MMH (L)**	**NTO (L)**
Molecular Weight [kg/kmol]	46.0717	92.011
Reference Temperature [K]	298.150	298.15
Specific Heat [J/K-mol]	134.930	142.509
Standard Entropy [J/K-mol]	165.940	209.198
Heat of Formation [kJ/mol]	54.140	19.564
Density [kg/m^3]	837.970	1443.000
Standard State Pressure [MPa]	-	0.1

Cold Flow Gas Species

When the model does not utilize any form of reacting chemistry, the cold flow is defined by the final gaseous products found from the MMH/NTO reaction. Hou et. al did not report specific quantities of the final products from the mixture reaction, so an alternative source for the gaseous species was found through Lee [10]. It must be noted that both works did not utilize the same reaction mechanisms, so mole fractions of the final products may vary, however, the final combustion temperature seen in the chamber are fairly similar. A very loose assumption is thus formed, where the presence of the products are assumed to be similar. The gas products, from Lee, utilized in the cold flow nozzle model are defined below in Table 3.4.

Computational Domain and Boundary Conditions

Due to the radially symmetrical nature of a thruster plume [1], the flow domain was simplified to an axisymmetric domain. The nozzle length is defined by the 164:1 length ratio for the R-4D-11 490 N thruster [20] and the extended domain (portion of the flow domain past the nozzle

Table 3.4: Mole Fractions of Combustion Products

Combustion Products Gas Species	**Mole Fractions**
H_2	0.15657
N_2	0.30513
H_2O	0.32741
CO	0.13145
CO_2	0.03628
H	0.02133
NO	0.00235
O	0.00131
OH	0.01709
O_2	0.00108

exit plane) was arbitrarily defined to be approximately 1.5 times the length of the nozzle.

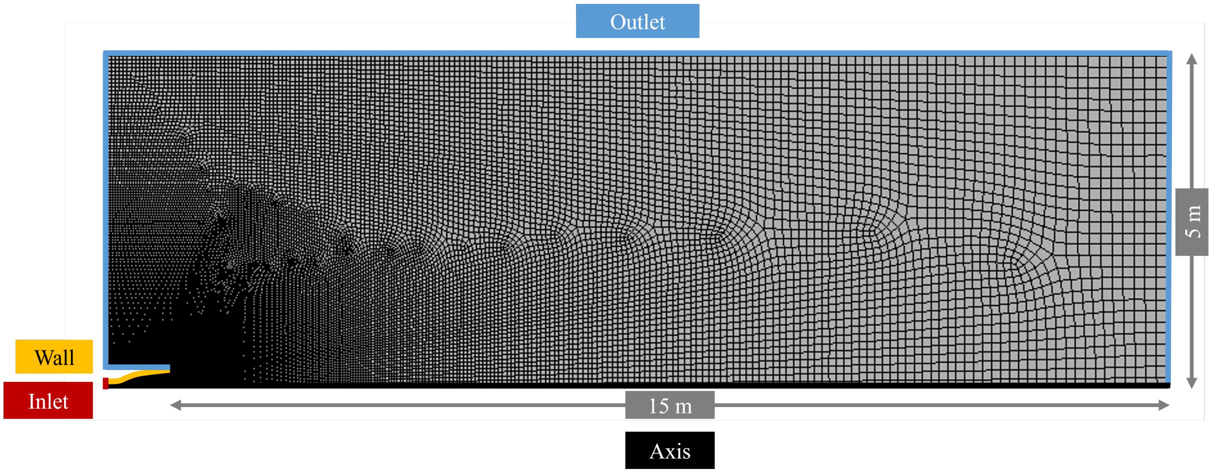

Figure 3.4: Computational Domain for Rocket Thruster Firing

Mesh refinements were made to the base mesh, Δx, where a one percent (1% or $0.01\Delta x$) refinement was generated in the full nozzle geometry and a tenth of a percent (0.1% or $0.001\Delta x$) refinement was generated in the nozzle's combustion chamber.

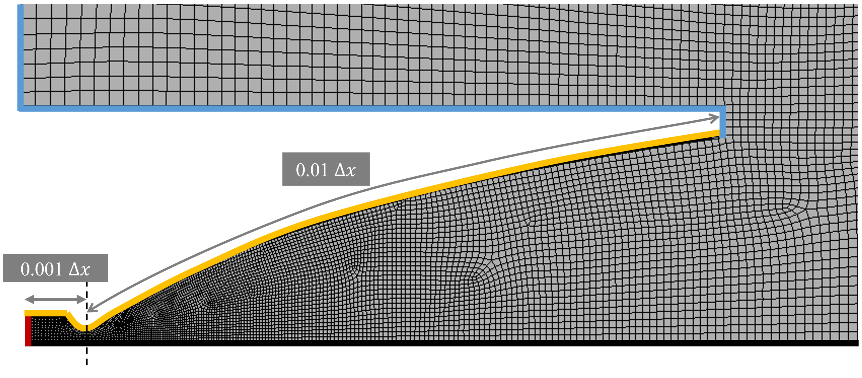

Figure 3.5: Regions of Refinement of Computational Domain

This flow domain was then split to identify the proper boundary conditions for the scenario. As seen in Figure 3.4, a mass flow inlet is prescribed at the inflow of the nozzle combustion chamber; a flow rate of 0.1606 kg/s was calculated from the nominal values of the 164:1 ratio R-4D-11 nozzle specification. The walls of the nozzle are specified to be adiabatic, no-slip walls. The extrapolated outlet conditions were set to a pressure outlet with a defined exit pressure of 0.0 Pa and an exit temperature of 0.0 K to mimic the low pressure and low temperature environment that defines space. The entire domain is initialized with no velocity and a ”ghost species” of gaseous helium, He, at 0.001 Pa and 0.001 K to also mimic the low density, pressure, and temperature of the space environment while avoiding any possible solving errors, such as divide by zeroes.

Prior to the application of reacting flow to the nozzle geometry, an initial validation of the simplified reacting mechanism is completed in STAR-CCM+ using a ”one-cell” geometry, as seen in Figure 3.6. The 0.1 m by 0.1 m axisymmetric cylinder was defined by an axis and adiabatic no-slip walls. The domain is initialized with a 1:1.0275:1.4725 molar ratio of gaseous MMH:NTO:NO_2 at 24,200 Pa and 298.15 K, defined in Hou et. al’s mechanism validation case [11]. Data is extracted from a vertical, linear probe of 50 points through the middle of the cell.

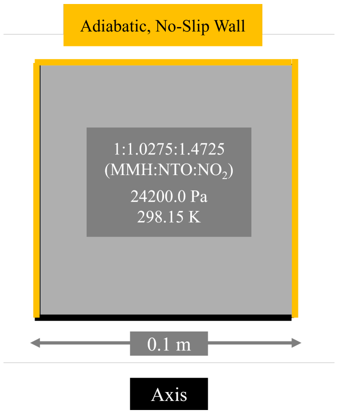

Figure 3.6: Computational Domain of One-Cell Validation

Similar to the nozzle and extended domain model, for the axisymmetric, nozzle-only domain of the reacting flow methodology, the domain is divided into such, as seen in Figure 3.7. An extension of an approximately 0.1 m axisymmetric cylindrical chamber was added by the inlet as a recreation of the total length of the combustion chamber for the R-4D-11 nozzle. Because the focus for this domain is the reaction process within the combustion chamber, refinement at the chamber region is critical. It is to note that all aforementioned mesh refinements and boundary conditions for the nozzle and extended domain geometry also apply to this domain. Due to the drop in temperature in the flow downstream, reactions may be neglected [8] so the computational domain for this reacting nozzle is split in two, halfway through the diverging portion with an internal interface specified at the contacting faces; the upstream portion of the domain includes active chemical reactions while the downstream portion, by the nozzle exit plane, is non-reacting.

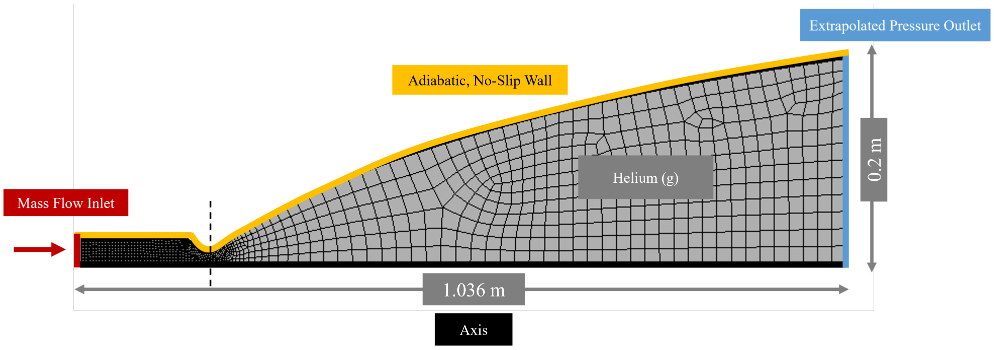

Figure 3.7: Computational Domain of Reacting Nozzle

CHAPTER 4: RESULTS AND DISCUSSIONS

Mesh Independence Study

To ensure properties and analysis of the flow scenario were independent of the mesh refinement level, a mesh independence study was performed for the flow domain consisting of the nozzle and the extended domain. With the understanding from Richardson's extrapolation, only three mesh sizes were selected for analysis. At a base mesh size of 2, 1, and 0.5 meters, integrated properties of density, temperature, and x- and y-velocity of the flow, all in relation to the radial distance from the nozzle throat, were extracted from the nozzle exit plane. Note that the aforementioned refinements applied in the nozzle domain and in the combustion chamber are still implemented and dependent on the three mesh sizes presented.

Table 4.1: Total Number of Cells in Fluid Domain for Mesh Study

Base Mesh Size, Δx [m]	**Total Number of Cells in Fluid Domain**
2.0	34,482
1.0	47,518
0.5	87,874

In Figure 4.1, non-conservative fluid properties of density, temperature, x-velocity, and y-velocity are plotted against a normalized nozzle exit radius to observe the behaviors between the refinement levels, where a $\frac{r}{r_0}$ value of one (1) indicates a position nearest to the nozzle wall while a value of zero (0) refers to the centerline of the axisymmetric domain.

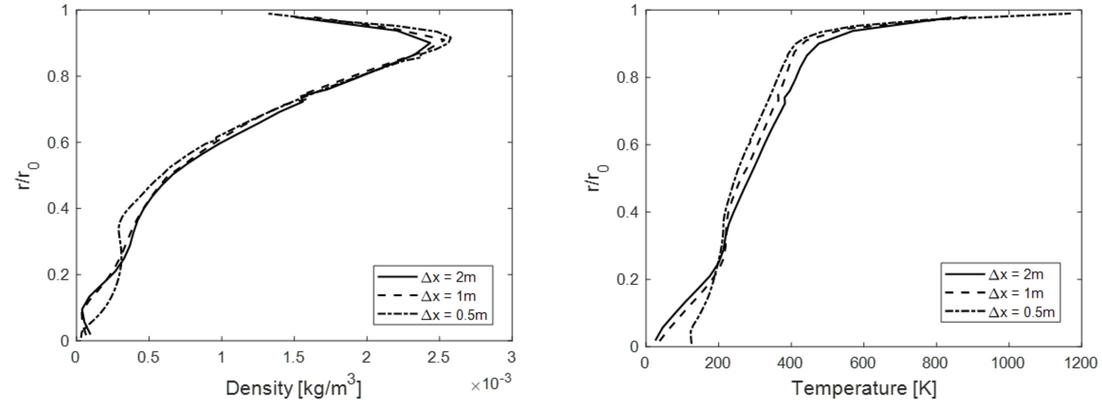

(a) Density (b) Temperature

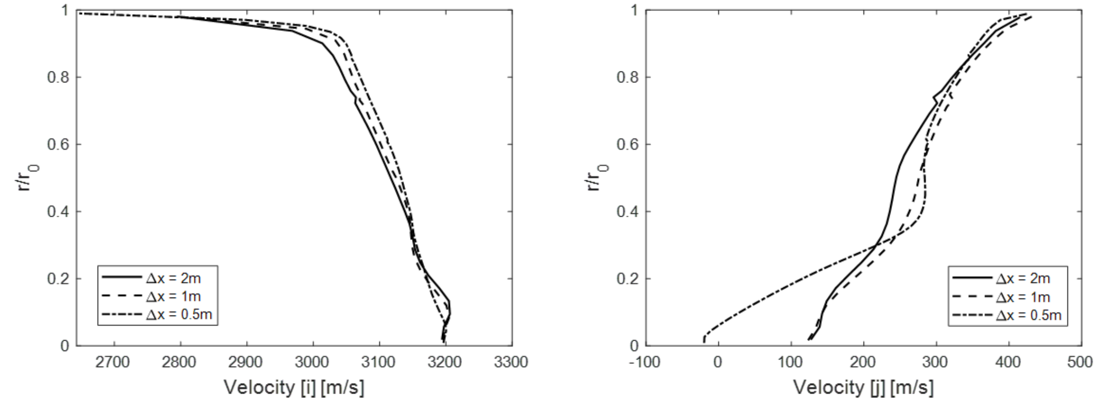

(c) X-Velocity (d) Y-velocity

Figure 4.1: Flow Properties at Nozzle Exit Plane

It can be observed that despite the increasing mesh refinements, the behaviors of the flow properties are extremely similar to one another for the R-4D-11 simulation. Figure 4.2 looks a little closer at the sensitivity of the solution to the mesh size at three points along the normalied nozzle exit radius: close to the centerline at 0.018, halfway to the nozzle wall at 0.470, and near the nozzle wall at 0.978.

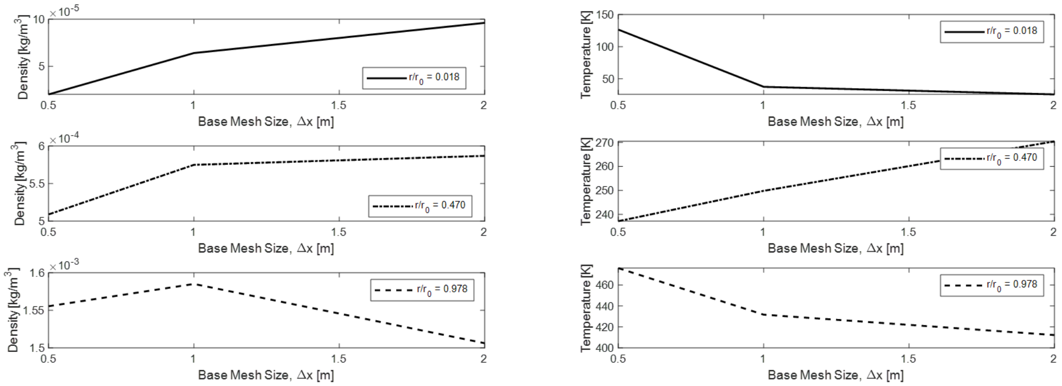

(a) Density

(b) Temperature

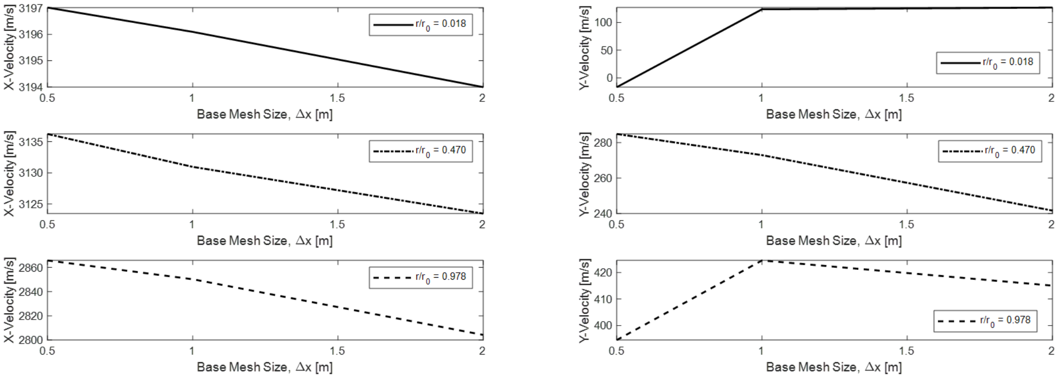

(c) X-Velocity

(d) Y-velocity

Figure 4.2: Density, Temperature, and Velocities at Different Levels of Refinement

Notice that for density, temperature, and x-velocity, the overall refinement to the computational domain does little to affect each of the properties shown; the values of density, temperature, and x-velocity present an asymptotic behavior. In terms of y-velocity, there are drastic differences in behavior with refinement. When observing the coarser and the mid-level refinement, it may suggest that the mesh size has not impacted the solution to a large extent. However, at the higher refinement level, the flow property evidently differs, specifically traveling away from the nozzle wall; this variance is much more evident in Figure 4.1(d) as the y-velocity for the finest mesh appears to be solved to be larger in comparison to the other levels, and a inwards (to the centerline) flow is indicated near the centerline. In a later section of comparing these results to literature, this negative y-velocity near the centerline is unexpected thus the input for the simulation at that refinement level needs to be re-evaluated and will, for this work, not be considered as accurate. Overall, as presented, this mesh study generally proves that the refinement level of the computational mesh is independent of the solved flow. In consideration of the computational cost, the domain with the coarsest mesh at a base size of 2 m is selected due to its ability to capture the flow as detailed as its finer counterparts.

Cold Flow Nozzle and Extended Domain

For the cold flow scenario where gas products of MMH/NTO in chemical equilibrium and liquid MMH/NTO particles are injected into the domain, the simulation was first run at steady-state with no particles. Data was taken for the last 1,000 iterations to calculate the mean and variance of each of the residuals in Table 4.2 to ensure convergence.

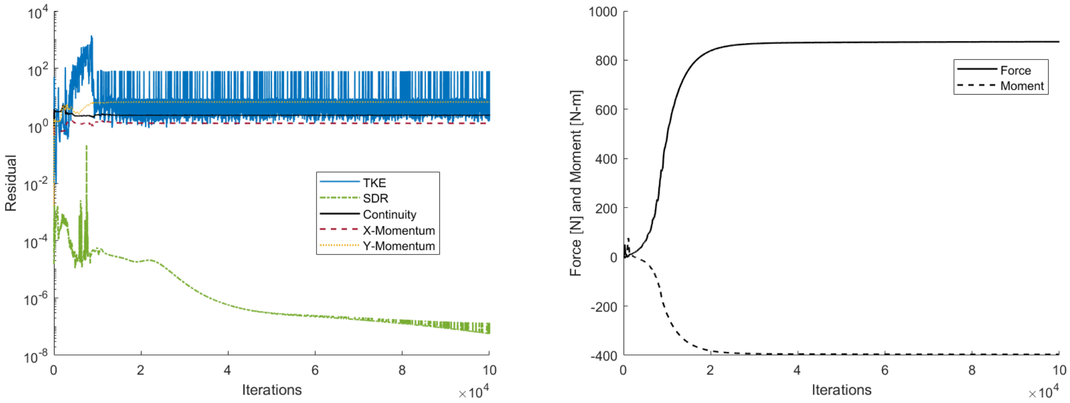

Figure 4.3: Residuals and Forces and Moments Convergence Data

Table 4.2: Residual Convergence Data

Residual	**Mean**	**Variance**
Continuity	4.87 E-04	4.46 E-11
X-Momentum	1.29 E+00	5.73 E-09
Y-Momentum	2.35 E-01	9.46 E-08
Turbulent Kinetic Energy (TKE)	1.65 E-02	1.53 E-03
Specific Dissipation Rate (SDR)	4.53 E-01	1.38 E-02

In Figure 4.3, the residuals reaching their respective asymptote suggests that the simulation is converged by the time it has reached 100,000 iterations. Similarly, the variances in Table 4.2 are multiple orders of magnitude less than the average values of each residual, confirming the convergence of the solution. TKE and SDR, although not as drastic, also see a lower magnitude of variance in comparison to their average. Figure 4.3 also presents the forces and moments monitored on the nozzle walls over the iterations; with observing forces approaching an asymptote of around 875 N and moment approaching an asymptote of around -397 N-m, convergence of the simulation is supported. Overall, the steady-state simulation has converged so implementing an unsteady solution over the existing fields will allow for improved convergence of the unsteady simulation.

Prior to such unsteady implementation, a further look at the flow behaviors in comparison to what may be observed in literature is considered. If the observations of the cold flow solutions at the exit plane are compared to what was calculated in literature for a reacting flow nozzle [10], the following can be analyzed in Figure 4.4.

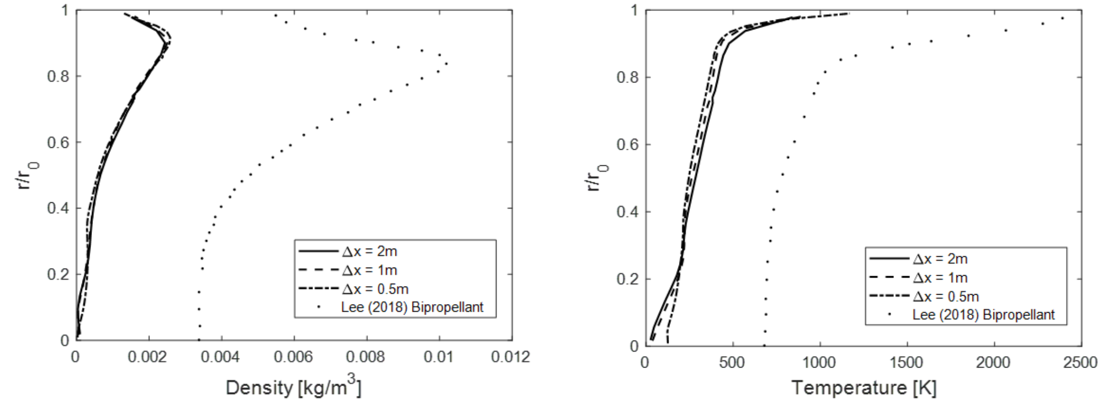

(a) Density (b) Temperature

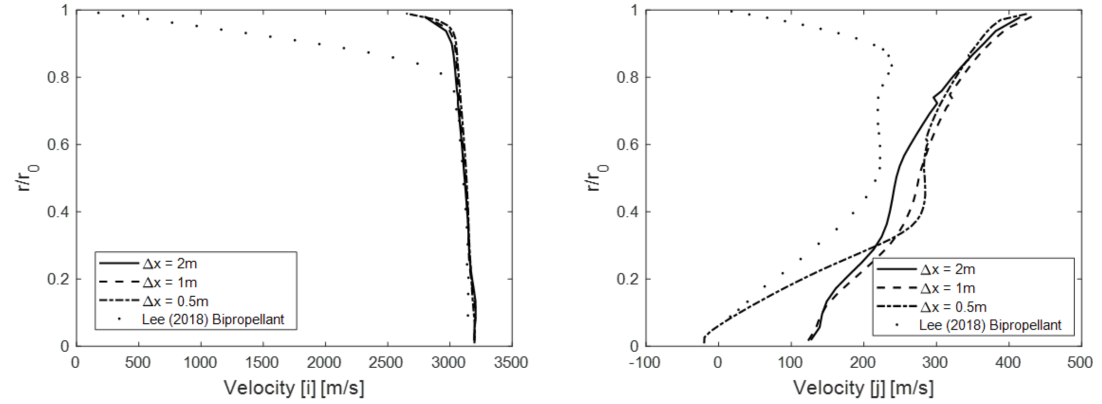

(c) X-Velocity (d) Y-velocity

Figure 4.4: Flow Properties at Nozzle Exit Plane as Compared to Lee [10]

As a reminder, in Lee's computation, reacting flow was considered in the inflow portion. In general, the behaviors of the fluid properties are captured fairly well in the STAR-CCM+ cold flow methodology despite the difference in inflow implementation. However, it is important to note the magnitudes of difference observed between density and temperature; with the inflow implementation being the most significant difference between the methodology and literature, it may be appropriate to suggest that active reactions play a significant role in calculating non-conservative fluid properties downstream of the inflow.

With the time-dependent simulation over the steady-state fields for cold flow, liquid Lagrangian particles are injected at the inlet with the specifications laid out in Table 3.3. In the Eulerian-Lagrangian framework, it is important to consider the drag of the discrete particles, thus the drag models discussed in the Methodology section were implemented and compared; parity plots between the added drag model into the simulation with the analytical equation are provided in the Appendix to validate implementation. The simulation of the R-4D-11 nozzle was run through a little over 1,000 time steps with each drag model to allow for the particles to travel at least halfway through the extended domain section. Using the resultant flow properties from the simulation, the following relationships of Reynolds number and drag coefficient were calculated and plotted for 20 different Mach numbers experienced by the particles.

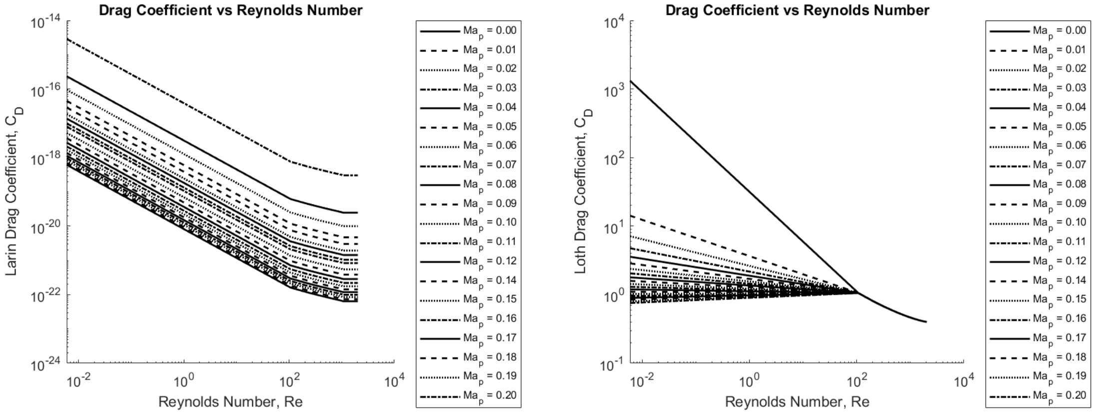

(a) Larin Drag Model (b) Loth Drag Model

Figure 4.5: Calculated Drag Coefficients from Simulation Values

Taking a closer look at the implemented Larin et. al model in the simulation, particle behavior is plotted and presented against the general behavior for drag as a function of Reynolds number, Re, and rarefaction coefficient, C_{Kn}, as a function of Knudsen number.

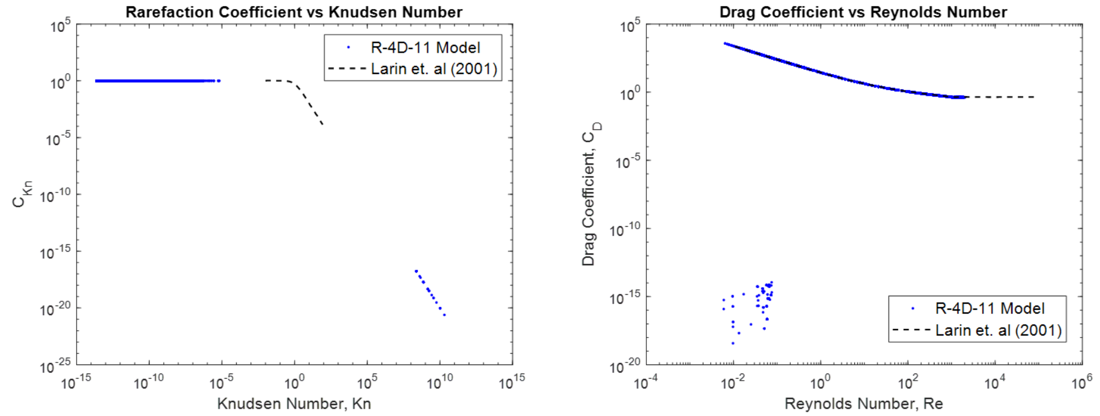

(a) Rarefaction Coefficient vs Knudsen Number (b) Drag Coefficient vs Reynolds Number

Figure 4.6: Rarefaction Coefficient and Drag Coefficient as Calculated from Larin

As seen in Figure 4.6, the behavior for the rarefaction coefficient presents as expected when applying the Larin et. al model to the simulation; as Knudsen number increases, the rarefaction coefficient decreases. This ease in similarity is due to the coefficient's sole dependency on the Knudsen number of the particle. It should be noted that particles within the regime between continuum and rarefied (i.e. slip and transitional) were not present in the domain when data was extracted, so this region is not properly represented in the simulation. When observing the drag coefficient, particles generally behave as expected within the flow domain, however, certain particles captured in the flow domain noticeably fall outside of the general drag-Reynolds number behavior. Specifically, these particles at lower Reynolds numbers experienced a reduced order of magnitude in drag than was to be expected.

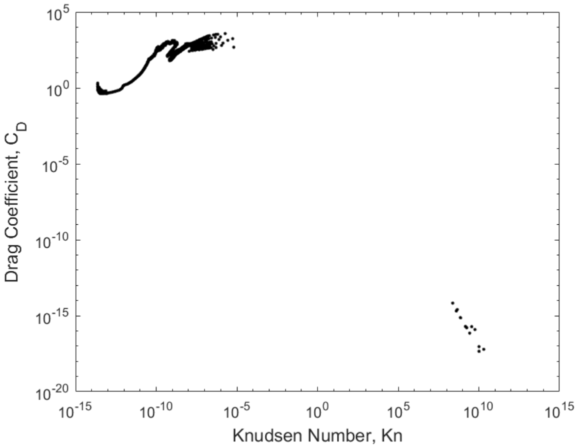

Figure 4.7: Larin Drag Model Relative to Knudsen Number

This deviation from the expected drag behavior was analyzed for both of the drag model's dependencies on Reynolds and Knudsen number, seen in Figure 4.7 and Figure 4.6(b). It appears that for particle Knudsen numbers multiple orders of magnitude larger than the general trend, the particle Reynolds number reduces to an order of magnitude of 10^{-1} and below. No explicit trends could be determined for the particles at larger Knudsen numbers from the data shown. Upon further inspection of the flow, this may be due to the continuous phase of the flow presenting lower than expected pressures (observing the minimum pressure of the domain to be just slightly negative) of which the calculation of C_{Kn}, a modifier within the drag constant, is dependent on. This may be considered due to the presence of a few particles with Knudsen numbers at an order of magnitude of 10.

With the unsteady model, the supersonic drag model from Loth et. al was also implemented in hopes of providing a better suited definition to the behavior of particles in the low density environment of space—specifically at those larger Knudsen numbers.

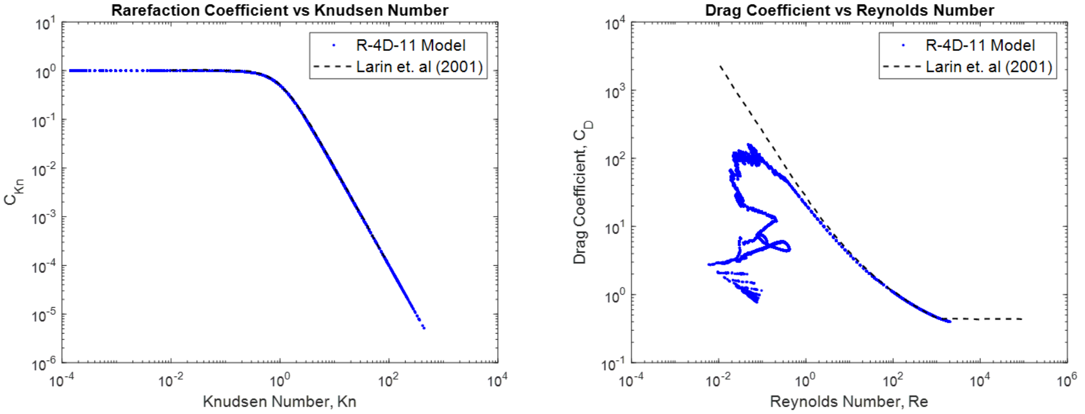

(a) Knudsen Number vs Rarefaction Coefficient (b) Reynolds Number vs Drag Coefficient

Figure 4.8: Rarefaction Coefficient and Drag Coefficient as Calculated from Loth

The behaviors of rarefaction coefficient and drag coefficient from Larin et. al are still utilized as comparison. Similar trends for both coefficients are found here as well, including particles which are outliers from the expected behavior.

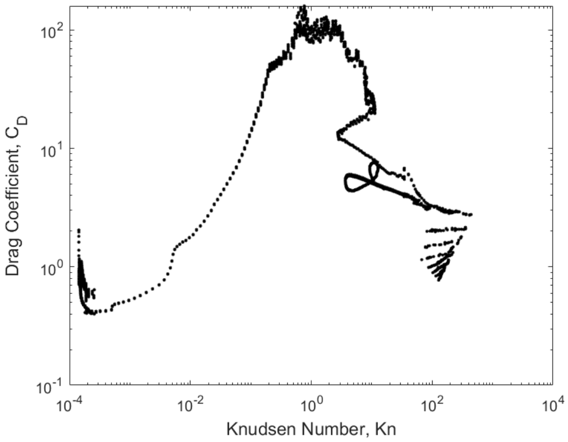

Figure 4.9: Loth Drag Model Relative to Reynolds Number and Knudsen Number

Figure 4.9 presents the coefficient of the Loth et. al drag behavior with dependencies on Reynolds number and Knudsen number. For particles experiencing a higher Knudsen number up to three orders of magnitude larger than the literature behavior, the particles also experience a much lower Reynolds number.

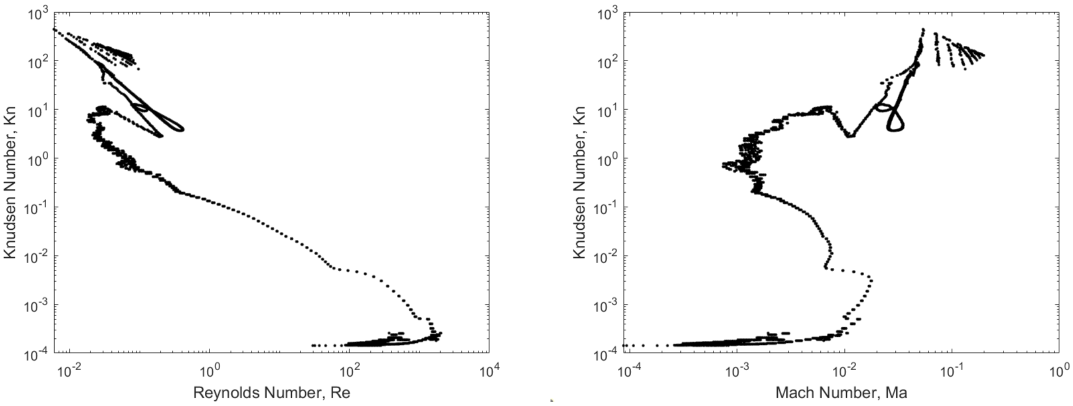

Figure 4.10: Loth Drag Model Dependencies

When observing a dependence on the Mach number, particles for some Knudsen number with a relatively higher Mach number experience a lower Reynolds number due to the inverse relationship between the two. Overall, from the data presented, it may be observed that as flows become rarefied in this continuum model (therefore larger Knudsen values), the Reynolds number of the particle drastically decreases and drag behaviors are not able to be accurately captured with the models studied. This observation may be attributed to the inabilities of the RANS continuum solver to capture flows with Knudsen numbers beyond 0.01—the general threshold for continuum flow as mentioned earlier on. However, a better understanding and visualization of the dependencies of the calculated Knudsen number should be considered for a better understanding.

Understanding Droplet Number Flux from Literature Numerical Models of Droplet Behavior

Recalling the droplet behavior models introduced by Larin et. al, specifically droplet number flux (Equation 2.1), nominal values of the R-4D-11 may be applied to understand what one may expect from a simulation. By using the initial values proposed by Larin for the range of droplet diameters and the droplet size distribution parameter, Figure 4.11(a) and Figure 4.11(b) present what is to be expected for the R-4D-11 when 10 meters away from the nozzle exit plane and up to 60 degrees away from the nozzle centerline.

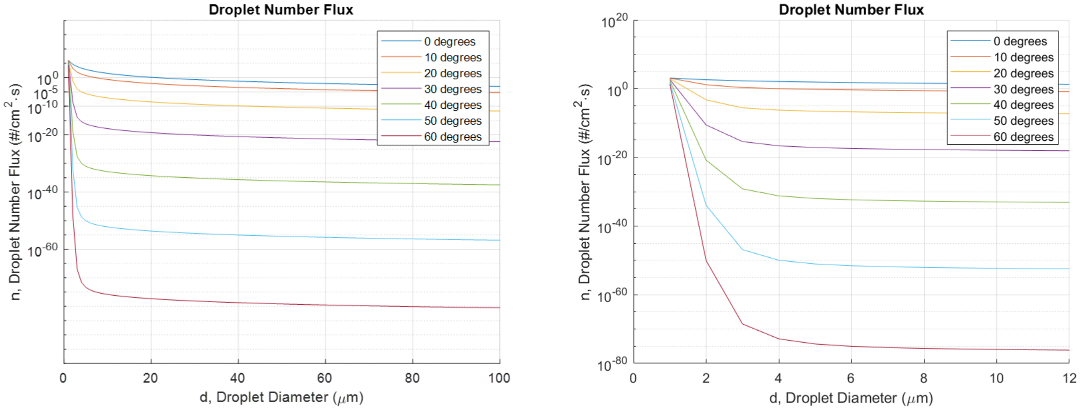

(a) Larin et. al Parameters

(b) Soares et. al Parameters

Figure 4.11: Droplet Number Flux for Nominal R-4D-11 Conditions

Notice with utilizing the Larin et. al parameters the trivial amount of particles larger than 10μm as compared to smaller particle sizes less than 10μm, which exist at an order of magnitude closer to 10^0. In tandem, it is evident that by around 20 to 30 degrees away from the centerline, the magnitude of droplet number flux rapidly approaches negligible values. By updating with parameters from Soares et. al to better match the SPIFEX and PIC experiments, similar observations may still be made. However, now with a decreased distribution parameter and decreased range of significant droplet diameters, the presence of larger particles are clearly seen to be of little value because by around 3μm, the flux is already less than 10^{-60}, an extremely small amount of particles overall.

To observe one parameter implementation to the simulation, one may consider the original definitions set by Larin et. al, at a arbitrary distance of 10 m. All particles at that point and beyond in the simulation may be plotted and presented here in Figure 4.12. Droplet sizes ranging from 1 µm to 100 µm was specified at the inlet with a Roisin-Rammler distribution.

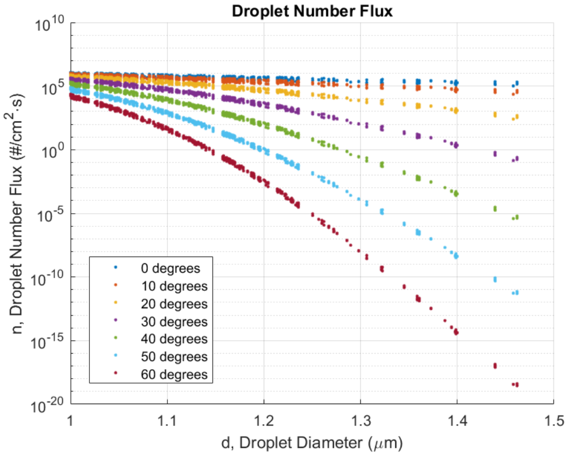

Figure 4.12: Droplet Number Flux Calculated at x = 10 m

Similar to what is observed in Figure 4.11(a), there is a large presence of droplets at a relatively small size, while there is less so of the relatively larger ones; the relation between angular distance away from the centerline and the presence of droplets are also similar. The main difference to note is that, thus far in the simulation run, only droplets up to 1.5 µm are present within the domain. A longer run time is required to further capture the remainder of the particle sizes that were specified at the beginning. However, thus far, the relationships of droplet number flux, diameter, and angle are reflective of what was expected of through the analytical calculations with the nominal values in Figure 4.11(a).

Reacting Chemistry Nozzle

Prior to implementation to any specific geometry, a validation of the implementation of the simplified reaction mechanism to STAR-CCM+ is completed. The simple ”one-cell” simulation described earlier in the Methodology was performed with gaseous states of the bipropellant fuel; the species thermodynamic properties are mentioned in the Appendices. In the first approach, where the low temperature was 300 K, the following can be observed by an extraction of data from the probe at the middle of the cell.

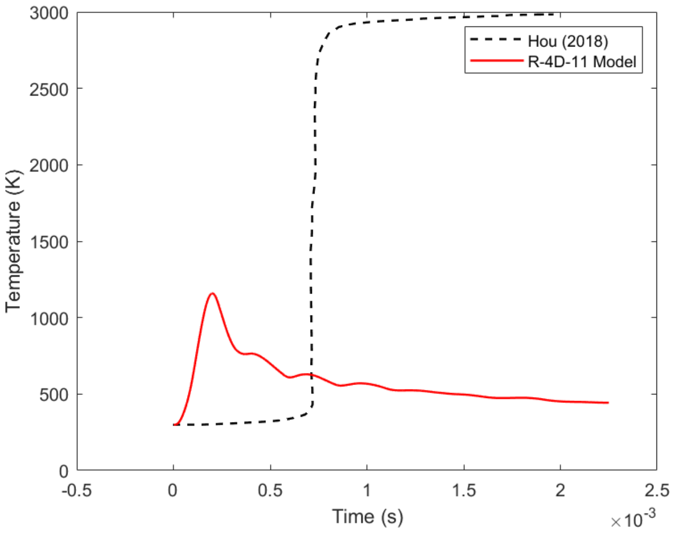

Figure 4.13: Temperature for One-Cell Geometry: 300 K Low

In Figure 4.13, the temperature of the simulation cell behaves as expected at the beginning with a room temperature of 298.15 K. However, as time continues, the temperature quickly hits a peak above 1,000 K; from there on, the temperature decreases to approximately 500 K. The behavior of the simulation past the first 0.2 ms of the recorded reaction does not reflect what is to be expected with the sharp increase mid-way through to high-temperature combustion of around 3,000 K. Observing this behavior over a longer duration of time, the temperatures continued as such and were unable to reach high-temperature combustion within 1 second. To further analyze what may be occurring, the mole fractions of specific products may be tracked and observed during this process.

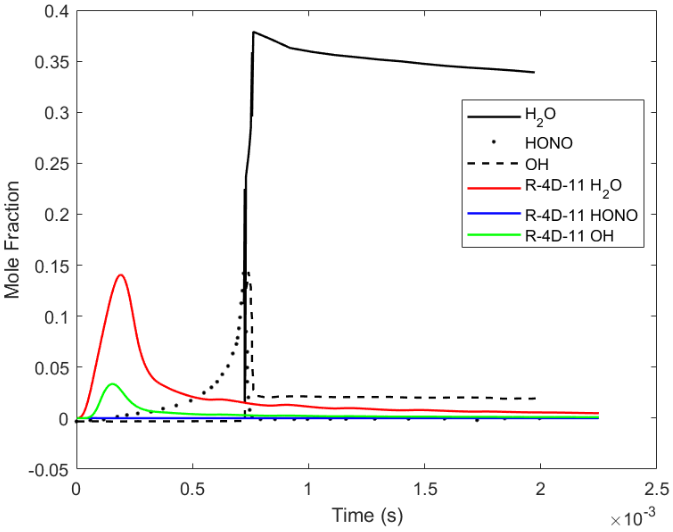

Figure 4.14: Mole Fractions for One-Cell Geometry: 300 K Low

Mentioned previously, Hou, Fu, and Ba pinpointed the major product species of the reaction are HONO, OH, and H_2O. The presence of these species is plotted in Figure 4.14 to compare with what was observed in literature. It is evident that at the beginning of the reaction process, no moles of such species exist. HONO is the first species present as MMH/NTO move and mix through the cold reaction phase and high-temperature pyrolysis occurs; only at hypergolic ignition around 0.7 ms do OH and H_2O appear and drastically increase; beyond to high-temperature combustion, H_2O, is most significantly present while the other two species are either negligible or greatly reduced. However as seen in Figure 4.14, the presence of the moles of all three species in the validation simulation do not mimic what is to be expected. This signifies the erroneous implementation of the reacting species and the collection of the species' thermodynamic properties at the same and correct temperature conditions requires further exploration.

In the second approach, with species defined at a low temperature of 200 K, the following may be observed for temperature behaviors.

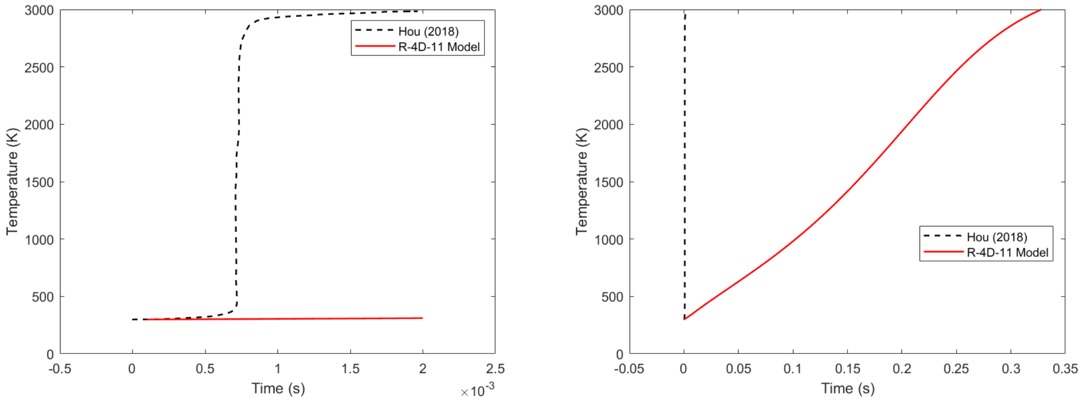

(a) Temperature Up to 2 Milliseconds (b) Temperature Up to 350 Milliseconds

Figure 4.15: Temperature for One-Cell Geometry: 200 K Low

For this approach, the temperature rise within 2 ms is not as noticeable, barely making it to above 300 K. However, in observing this reaction definition over a longer period of time, temperature increase at the middle of the cell does occur. After 0.3 s, the extracted temperature reaches the high-temperature combustion value of 3,000 K; looking further at this behavior, the reaction and temperature increase process appears approximately linear, unlike what was to be expected and is defined by Hou et. al.

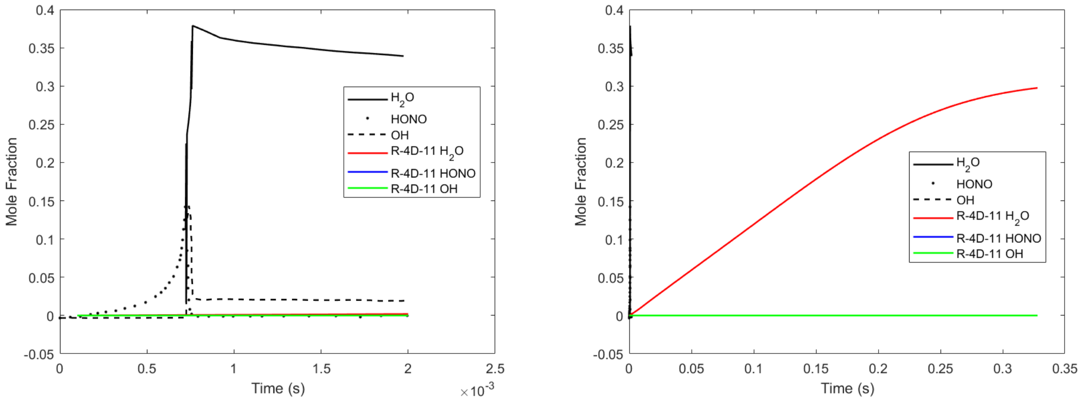

(a) Mole Fractions Up to 2 Milliseconds

(b) Mole Fractions Up to 350 Milliseconds

Figure 4.16: Mole Fractions for One-Cell Geometry: 200 K Low

In terms of the mole fractions of the significant species, Figure 4.16 presents similarly insufficient results. The species of H_2O, HONO, and OH are relatively negligible during the observed time range of 2 ms with no significant increase in mole fractions. Observing this trend over a longer portion of time as well, the most significant species of H_2O does show an increase in mole fractions to approximately 0.3—fairly similar to the behavior defined in Hou et. al's work; HONO and OH, on the other hand, remain relatively negligible through this period of time, with no significant increase in mole fractions. It is promising to observe the temperature and H_2O increase for this approach in the species, however, this required an extended time period for these parameters to behave as they did and was still unable to capture the sudden jump in temperature or mole fractions that should be expected during the process. Similar to the first approach, this signifies an erroneous implementation of the reacting species and the collection of the species' thermodynamic properties. The process of the reaction and the length in the time of the reaction needs to be further studied.

Due to this validation simulation not being able to produce the intended results, the implementation to the reacting nozzle computational domain, at this moment, will be unable to provide any results of significance. Implementation to the nozzle domain will need to be considered in future work.

CHAPTER 5: CONCLUSION

Overall, this work has presented models to implement into a working cold flow CFD simulation with injected liquid fuel particles, studied implementation of drag models for the liquid particles in a varying Knudsen number environment, and presented a validation case for reacting flow implementation in STAR-CCM+.

Flow properties at the nozzle exit plane for the cold flow method were compared against a literature's reacting model, presenting significant differences between some of the properties. It is observed that active reactions implemented at the inflow conditions for the simulation play a significant role in downstream calculations of non-conservative flow properties, such as density and temperature.

From the two drag models implemented in this study, Larin et. al and Loth et. al, calculations of the particles' drag as it relates to the particles' Knudsen numbers suggest that Loth et. al's model may be more applicable to the R-4D-11 simulation. However, further clarifications in the behaviors of the dependencies in the flow regime are needed.

The numerical model of droplet number flux was discussed in terms of the nominal conditions for an R-4D-11 thruster for both Larin et. al and Soares et. al parameters. The unsteady simulation, with the Larin et. al implementation of parameters, presents similar behaviors of droplet presence at a distance of 10 m away, however, a longer simulation run time may need to be considered to capture the remainder of the droplet diameter distribution specified at the inlet.

The simple 23-species, 20-reactions mechanism implemented into STAR-CCM+ requires revision as temperatures in the observed cell are not reaching the desired high-temperature combustion phase during the intended range of time and the irregular presence of significant gaseous species indicate an erroneous reaction process.

In future work, the implementations of additional drag models and behaviors in the converged cold flow field shall be studied to determine the most accurate drag model for this Eulerian-

Lagrangian approach in the given environment. Droplet number flux and droplet velocities may be further analyzed after normalization and at multiple distances from the nozzle exit plane—behaviors shall be compared one-to-one with the notional model with nominal conditions of the R-4D-11. Further validation work in the implementation of reacting chemistry into STAR-CCM+ is of utmost importance as a means to provide more accurate inflow conditions; continuation of gas-only reactions to compare to expected behaviors shall be completed before transforming the gaseous one-cell validation case to injected reacting liquid particles. Addition of the validated reaction process to the reacting nozzle computational domain to analyze the scalars of significant flow properties (e.g. pressure, temperature, and moles of significant reactors and products) will further prove the proper function of reactions to the simulation. Ultimately, with a validated liquid combustion process, the implementation to the working cold flow domain shall provide further accuracy to the development of this STAR-CCM+ continuum model for comparison to transient droplet data from the ground experiments of RCS thrusters.

APPENDIX A: ADDITIONAL PLOTS OF DRAG IMPLEMENTATION ANALYSIS

The following provides additional plots for further understanding in the implementation of the drag models to the STAR-CCM+ simulation.

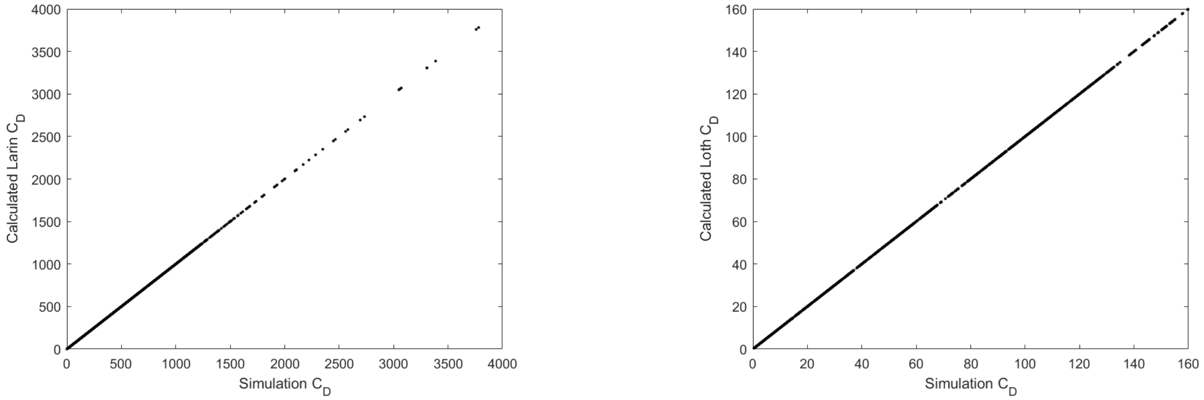

Figure A.1: Parity Plots for Larin Drag Model and Loth Drag Model Implementation into STAR-CCM+

APPENDIX B: THERMOCHEMISTRY FOR REACTING FLOW

Chemkin Format File for 23 Species, 20 Reactions Simplified Mechanism from Hou et. al[11] Using a 300 K Low Temperature Specification

```
ELEMENTS
 H C N O
END
!------------------------------------------------------------------------
SPECIES
 CH2O CH3 CH3N2 CH4N2 CH5N2 CH6N2
 CN CO CO2
 H H2 H2O HONO HCN HCO
 N2 N2O4 NH NH2 NO NO2
 O OH
END
!------------------------------------------------------------------------
THERMO ALL
    300.000 1000.000 5000.000
CH2O  121286C lH 20 1 G  300.00 5000.00 1000.00 1
 0.02995606E+02 0.06681321E-01 -0.02628954E-04 0.04737153E-08 -0.03212517E-12 2
-0.15320369E+05 0.06912572E+02 0.16527311E+01 0.12631439E-01 -0.01888168E-03 3
 0.02050031E-06 -0.08413237E-10 -0.14865404E+05 0.13784820E+02  4
CH3 121286C 1H 3 G  300.00 5000.00 1000.00 1
 0.02844051E+02 0.06137974E-01-0.02230345E-04 0.03785161E-08 -0.02452159E-12 2
 0.16437809E+05 0.05452697E+02 0.02430442E+02 0.11124099E-01 -0.01680220E-03 3
 0.16218288E-07-0.05864952E-10 0.16423781E+05 0.06789794E+02 4
CH3N2 CH3N=N* T 9/96C 1H 3N 2 G 200.000 6000.000 B 43.04830 1
 0.57393539E+01 0.92314020E-02-0.33396566E-05 0.54160230E-09 -0.32522545E-13 2
 0.27235968E+05 -0.53905119E+01 0.46506054E+01 -0.14932994E-02 0.37619849E-04 3
-0.46522472E-07 0.17885496E-10 0.28216313E+05 0.35837652E+01 0.29785394E+05 4
CH4N2 DIEVARC 1N 2H 4 G 100.000 5000.000 1000.00 1
 3.95629400E+00 1.38013171E-02 -5.46584120E-06 9.95396112E -10-6.83102150E-14 2
 1.91288683E+04 4.04039625E+00 4.18463863E+00 9.41702628E-04 3.17429343E-05 3
-3.57566902E-08 1.21062703E-11 1.96805112E+04 5.92532438E+00 4
CH5N2 CH3N*NH2 T 9/96C 1H 5N 2 G 200.000 6000.000 B 45.06418 1
 0.62727186E+01 0.13750206E-01-0.48829875E-05 0.78213769E-09-0.46564024E-13 2
 0.22861878E+05 -0.96381311E+01 0.42113439E+01 0.34130124E-02 0.41788037E-04 3
-0.55495848E-07 0.21958966E-10 0.24203232E+05 0.48609693E+01 0.25880433E+05 4
CH6N2 A10/04C 1H 6N 2 G 200.000 6000.000 B 46.07182 1
 6.63737309E+00 1.56702023E-02-5.47121574E-06 8.65945432E-10-5.11109616E-14 2
```

```
 9.95613633E+03 -1.05806558E+01 3.36546357E+00 9.16487019E-03 4.07415430E-05 3
-6.18270852E-08 2.62064026E-11 1.14982139E+04 9.75314576E+00 1.31591158E+04 4
CN   121286C lN 1 G 0300.00 5000.00 1000.00 1
 0.03720119E+02 0.15183506E-03 0.01987381E-05 -0.03798371E-09 0.13282296E-14 2
 0.05111626E+06 0.02888597E+02 0.03663204E+02 -0.11565290E-02 0.02163409E-04 3
 0.01854208E-08-0.08214695E-1l 0.05128118E+06 0.03739015E+02   4
CO 121286C 10 1 G 0300.00 5000.00 1000.00 1
 0.03025078E+02 0.14426885E-02-0.05630827E-05 0.10185813E-09-0.06910951E-13 2
-0.14268350E+05 0.06108217E+02 0.03262451E+02 0.15119409E-02-0.03881755E-04 3
 0.05581944E-07-0.02474951E-10-0.14310539E+05 0.04848897E+02   4
CO2   121286C 10 2  G 0300.00 5000.00 1000.00 1
 0.044536238+02 0.03140168E-01 -0.12784105E-05 0.02393996E-08 -0.16690333E-13 2
-0.04896696E+06 -0.09553959E+0l 0.022757248+02 0.09922072E-01 -0.10409113E-04 3
 0.06866686E-07 -0.02117280E-10 -0.04837314E+06 0.10188488E+02  4
H  120186H 1 G 0300.00 5000.00 1000.00 1
 0.02500000E+02 0.00000000E+00 0.00000000E+00 0.00000000E+00 0.00000000E+00 2
 0.02547162E+06-0.04601176E+0l 0.02500000E+02 0.00000000E+00 0.00000000E+00 3
 0.00000000E+00 0.00000000E+00 0.02547162E+06-0.04601176E+0l  4
H2  121286H 2  G 0300.00 5000.00 1000.00 1
 0.02991423E+02 0.07000644E-02-0.05633828E-06-0.09231578E-10 0.15827519E-14 2
-0.08350340E+04-0.13551101E+0l 0.03298124E+02 0.08249441E-02-0.08143015E-05 3
-0.09475434E-09 0.04134872E-11-0.10125209E+04-0.03294094E+02   4
H2O  20387H 20 1 G 0300.00 5000.00 1000.00 1
0.02672145E+02 0.03056293E-01 -0.08730260E-05 0.12009964E-09 -0.06391618E-13 2
-0.02989921E+06 0.06862817E+02 0.03386842E+02 0.03474982E-01 -0.06354696E-04 3
0.06968581E-07 -0.02506588E-10 -0.03020811E+06 0.02590232E+02  4
HONO  31787H 1N 10 2 G 0300.00 5000.00 1000.00 1
0.05486893E+02 0.04218065E-01 -0.01649143E-04 0.02971877E-08 -0.02021148E-12 2
-0.01126865E+06 -0.02997002E+02 0.02290413E+02 0.01409922E+00 -0.01367872E-03 3
0.07498780E-07 -0.01876905E-10 -0.01043195E+06 0.01328077E+03  4
HCN   1212868 lC 1N 1 G 0300.00 5000.00 1000.00 1
0.036500778+02 0.03460998E-01 -0.12742788E-05 0.02217655E-08 -0.14771774E-13 2
0.149839168+05 0.023932208+02 0.024904628+02 0.08611280E-01 -0.10310342E-04 3
0.07481498E-07 -0.02229109E-10 0.152083448+05 0.079049818+02  4
HCO   1212868 lC 10 1 G 0300.00 5000.00 1000.00 1
0.035572718+02 0.03345572E-0l -0.13350060E-05 0.02470572E-08 -0.01713850E-12 2
0.039163248+05 0.055522998+02 0.028983298+02 0.06199146E-01 -0.09623084E-04 3
0.10898249E-07 -0.04574885E-10 0.041599228+05 0.08983614E+02   4
N2   121286N 2  G 0300.00 5000.00 1000.00 1
```

```
0.02926640E+02 0.14879768E-02 -0.05684760E-05 0.10097038E-09 -0.06753351E-13 2
-0.09227977E+04 0.05980528E+02 0.03298677E+02 0.14082404E-02 -0.03963222E-04 3
0.05641515E-07 -0.02444854E-10 -0.10208999E+04 0.03950372E+02   4
N2O4   121286N 20 4  G 0300.00 5000.00 1000.00 1
0.10482201E+02 0.05972272E-01 -0.02564043E-04 0.04916885E-08 -0.03490969E-12 2
-0.02849988E+05 -0.02612289E+03 0.03624592E+02 0.02474708E+00 -0.02172874E-03 3
0.09927103E-07 -0.02222817E-10 -0.09128241E+04 0.09457174E+02   4
NH   31387H lN 1 G 0300.00 5000.00 1000.00 1
0.02760249E+02 0.13753463E-02 -0.04451914E-05 0.07692791E-09 -0.05017592E-13 2
0.04207828E+06 0.05857199E+02 0.03339758E+02 0.12530086E-02 -0.03491645E-04 3
0.04218812E-07 -0.15576179E-11 0.04185047E+06 0.02507180E+02 4
NH2   121686N 1H 2 G 0300.00 5000.00 1000.00 1
0.02961311E+02 0.02932699E-01 -0.09063600E-05 0.16172575E-09 -0.12042003E-13 2
0.02191976E+06 0.05777878E+02 0.03432493E+02 0.03299540E-01 -0.06613600E-04 3
0.08590947E-07 -0.03572046E-10 0.02177227E+06 0.03090110E+02  4
NO   121286N 10 1  G 0300.00 5000.00 1000.00 1
0.03245435E+02 0.12691383E-02 -0.05015890E-05 0.09169283E-09 -0.06275419E-13 2
0.09800840E+05 0.06417293E+02 0.03376541E+02 0.12530634E-02 -0.03302750E-04 3
0.05217810E-07 -0.02446262E-10 0.09817961E+05 0.05829590E+02  4
NO2   121286N 10 2 G 0300.00 5000.00 1000.00 1
0.04682859E+02 0.02462429E-01 -0.10422585E-05 0.01976902E-08 -0.13917168E-13 2
0.02261292E+05 0.09885985E+0l 0.02670600E+02 0.07838500E-01 -0.08063864E-04 3
0.06161714E-07 -0.02320150E-10 0.02896290E+05 0.11612071E+02   4
O  1201860 1 G 0300.00 5000.00 1000.00 1
0.02542059E+02 -0.02755061E-03 -0.03102803E-07 0.04551067E-10 -0.04368051E-14 2
0.02923080E+06 0.04920308E+02 0.02946428E+02 -0.16381665E-02 0.02421031E-04 3
-0.16028431E-08 0.03890696E-11 0.02914764E+06 0.02963995E+02   4
OH  1212860 lH 1 G 0300.00 5000.00 1000.00 1
0.02882730E+02 0.10139743E-02 -0.02276877E-05 0.02174683E-09 -0.05126305E-14 2
0.03886888E+05 0.05595712E+02 0.03637266E+02 0.01850910E-02 -0.16761646E-05 3
0.02387202E-07 -0.08431442E-11 0.03606781E+05 0.13588605E+0l 4
END
REACTIONS
!----------------------------------------------------------------------
!Reactions    A n Ea
!----------------------------------------------------------------------
N2O4 + M => NO2 + NO2 + M  1.960E+28 -3.800 12840.00
CH6N2 + NO2 => CH5N2 + HONO  2.200E+11 0.000 6700.00
CH5N2 + NO2 => CH4N2 + HONO  1.000E+08 2.000 0.00
```

```
CH4N2 + NO2 => CH3N2 + HONO  2.200E+11 0.000 6700.00
CH6N2 => CH4N2 + H2   3.260E+13 0.000 18700.00
HONO + M => NO + OH + M   8.400E+12 0.000 17000.00
NO2 => NO + O    0.760E+19 -1.270 73290.00
NO2 + H => NO + OH   0.350E+15 0.000 1500.00
CH3N2 => CH3 + N2   3.000E+06 0.000 0.00
H2 + OH => H2O + H   2.160E+10 1.510 0.00
CH3 + O => H + CH2O   8.430E+13 0.000 0.00
CH2O + O => OH + HCO   3.900E+13 0.000 3540.00
HCO + O => H + CO2   3.000E+13 0.000 0.00
CH3 + NO => HCN + H2O   9.600E+13 0.000 28800.00
HCN + M => H + CN + M   1.040E+29 -3.300 126600.00
CN + H2 => HCN + H   2.100E+13 0.000 4710.00
NH2 + H => NH + H2   4.000E+13 0.000 3650.00
NH + NO => N2 + OH   2.160E+13 -0.230 0.00
H2 + O => H + OH   5.060E+04 2.670 6290.63
HCN + OH => NH2 + CO   1.600E+02 2.560 9000.00
END
```

Chemkin Format File for 23 Species, 20 Reactions Simplified Mechanism from Hou et. al[11] Using a 200 K Low Temperature Specification

```
ELEMENTS
 H C N O
END
!-----------------------------------------------------------------------
SPECIES
 CH2O CH3 CH3N2 CH4N2 CH5N2 CH6N2
 CN CO CO2
 H H2 H2O HONO HCN HCO
 N2 N2O4 NH NH2 NO NO2
 O OH
END
!-----------------------------------------------------------------------
THERMO ALL
  200.000 1000.000 6000.000
CH3 IU0702C 1.H 3. 0. 0.G 200.000 6000.000 1000. 1
 0.29781206E+01 0.57978520E-02-0.19755800E-05 0.30729790E-09-0.17917416E-13 2
 0.16509513E+05 0.47224799E+01 0.36571797E+01 0.21265979E-02 0.54583883E-05 3
```

```
-0.66181003E-08 0.24657074E-11 0.16422716E+05 0.16735354E+01 0.17643935E+05 4
CH3N2 C*H2-N=NH T01/07C 1.H 3.N 2. 0.G 200.000 6000.000 1000. 1
 5.47076557E+00 9.11107856E-03-3.16313360E-06 4.99187144E-10-2.95473954E-14 2
 3.74667047E+04-3.19073080E+00 3.57029082E+00-1.48090274E-03 4.52661907E-05 3
-5.91771671E-08 2.37099386E-11 3.86912534E+04 1.02718494E+01 3.99840866E+04 4
CH3NHNH2 A10/04C 1.H 6.N 2. 0.G 200.000 6000.000 1000. 1
 6.63737309E+00 1.56702023E-02-5.47121574E-06 8.65945432E-10-5.11109616E-14 2
 9.95613633E+03-1.05806558E+01 3.36546357E+00 9.16487019E-03 4.07415430E-05 3
-6.18270852E-08 2.62064026E-11 1.14982139E+04 9.75314576E+00 1.31591158E+04 4
CH3NNH T01/07C 1.H 4.N 2. 0.G 200.000 6000.000 1000. 1
 5.16688109E+00 1.19659661E-02-4.22259088E-06 6.73714737E-10-4.00071972E-14 2
 2.60910645E+04-5.20599374E+00 4.31065208E+00-1.41445694E-02 9.03613959E-05 3
-1.10332632E-07 4.33491173E-11 2.75483275E+04 5.68200327E+00 2.88056316E+04 4
CH3NNH2 T02/07C 1.H 5.N 2. 0.G 200.000 6000.000 1000. 1
 6.77444120E+00 1.20667340E-02-4.19822074E-06 6.63042484E-10-3.90816977E-14 2
 2.24045907E+04-9.92485204E+00 3.34217170E+00 1.09604996E-02 2.39704529E-05 3
-4.06075001E-08 1.76012912E-11 2.37899807E+04 1.01530777E+01 2.54134481E+04 4
CH2O CH**-OH T 9/09C 1.H 2.O 1. 0.G 200.000 6000.000 1000. 1
 3.65237205E+00 5.55807060E-03-1.97617181E-06 3.16823378E-10-1.88747598E-14 2
 1.35536156E+04 4.22140840E+00 4.65733258E+00-9.53742306E-03 4.04679152E-05 3
-4.45317569E-08 1.64761516E-11 1.38615127E+04 1.97860732E+00 1.51034947E+04 4
COH IU5/03C 1.H 1.O 1. 0.G 200.000 6000.000 1000. 1
 4.23892214E+00 1.96576170E-03-3.82075171E-07 4.80137647E-11-3.11176347E-15 2
 2.47261645E+04 1.99698242E+00 4.36380907E+00-5.35204137E-03 2.31954508E-05 3
-2.66109040E-08 1.02711962E-11 2.50108717E+04 2.98106307E+00 2.62312512E+04 4
CO RUS 79C 1O 1 0 0G 200.000 6000.000 1000. 1
 0.30484859E+01 0.13517281E-02-0.48579405E-06 0.78853644E-10-0.46980746E-14 2
-0.14266117E+05 0.60170977E+01 0.35795335E+01-0.61035369E-03 0.10168143E-05 3
 0.90700586E-09-0.90442449E-12-0.14344086E+05 0.35084093E+01-0.13293628E+05 4
CO2 cy C(OO) T 2/12C 1.O 2. 0. 0.G 200.000 6000.000 1000. 1
 5.46657136E+00 1.54746903E-03-6.00720641E-07 1.01977083E-10-6.31785729E-15 2
 2.09000241E+04-3.59834582E+00 3.18455825E+00 5.36293068E-03 2.20597088E-06 3
-8.41226636E-09 4.16778552E-12 2.16324827E+04 8.74099016E+00 2.28251575E+04 4
CN IU8/03C 1.N 1. 0. 0.G 200.000 6000.000 1000. 1
 3.39912850E+00 7.46548662E-04-1.41493852E-07 1.86747736E-11-1.26032540E-15 2
 5.16569715E+04 4.67148681E+00 3.61256069E+00-9.53015737E-04 2.13757271E-06 3
-3.05001808E-10-4.70518097E-13 5.17084034E+04 3.98238722E+00 5.27611901E+04 4
HONO equil ATcT T 9/11H 1.N 1.O 2. 0.G 200.000 6000.000 1000. 1
 5.79182717E+00 3.65162554E-03-1.29293390E-06 2.06892796E-10-1.23154749E-14 2
```

```
-1.15953895E+04-4.05538852E+00 3.21415915E+00 8.12778066E-03 1.65998916E-06 3
-9.52814708E-09 4.87131424E-12-1.07830727E+04 9.82200056E+00-9.46538040E+03 4
H2 REF ELEMENT tpis78H 2. 0. 0. 0.G 200.000 6000.000 1000. 1
 2.93286575E+00 8.26608026E-04-1.46402364E-07 1.54100414E-11-6.88804800E-16 2
-8.13065581E+02-1.02432865E+00 2.34433112E+00 7.98052075E-03-1.94781510E-05 3
 2.01572094E-08-7.37611761E-12-9.17935173E+02 6.83010238E-01 0.00000000E+00 4
H L 6/94H 1 0 0 0G 200.000 6000.000 1000. 1
 0.25000000E+01 0.00000000E+00 0.00000000E+00 0.00000000E+00 0.00000000E+00 2
 0.25473660E+05-0.44668285E+00 0.25000000E+01 0.00000000E+00 0.00000000E+00 3
 0.00000000E+00 0.00000000E+00 0.25473660E+05-0.44668285E+00 0.26219035E+05 4
H2O L 5/89H 2O 1 0 0G 200.000 6000.000 1000. 1
 0.26770389E+01 0.29731816E-02-0.77376889E-06 0.94433514E-10-0.42689991E-14 2
-0.29885894E+05 0.68825500E+01 0.41986352E+01-0.20364017E-02 0.65203416E-05 3
-0.54879269E-08 0.17719680E-11-0.30293726E+05-0.84900901E+00-0.29084817E+05 4
HCN ATcT/AH 1.C 1.N 1. 0.G 200.000 6000.000 1000. 1
 3.80231648E+00 3.14630087E-03-1.06315727E-06 1.66185438E-10-9.79891962E-15 2
 1.42849502E+04 1.57501632E+00 2.25901199E+00 1.00510475E-02-1.33514567E-05 3
 1.00920479E-08-3.00880408E-12 1.45903166E+04 8.91631960E+00 1.56111424E+04 4
N2 REF ELEMENT G 8/02N 2. 0. 0. 0.G 200.000 6000.000 1000. 1
 2.95257637E+00 1.39690040E-03-4.92631603E-07 7.86010195E-11-4.60755204E-15 2
-9.23948688E+02 5.87188762E+00 3.53100528E+00-1.23660988E-04-5.02999433E-07 3
 2.43530612E-09-1.40881235E-12-1.04697628E+03 2.96747038E+00 0.00000000E+00 4
NH2 AMIDOGEN RAD IU3/03N 1.H 2. 0. 0.G 200.000 3000.000 1000. 1
 2.59263049E+00 3.47683597E-03-1.08271624E-06 1.49342558E-10-5.75241187E-15 2
 2.18865421E+04 7.90565351E+00 4.19198016E+00-2.04602827E-03 6.67756134E-06 3
-5.24907235E-09 1.55589948E-12 2.14991387E+04-9.04785244E-02 2.27072912E+04 4
NH ATcT/AN 1.H 1. 0. 0.G 200.000 6000.000 1000. 1
 2.78372644E+00 1.32985888E-03-4.24785573E-07 7.83494442E-11-5.50451310E-15 2
 4.23461945E+04 5.74084863E+00 3.49295037E+00 3.11795720E-04-1.48906628E-06 3
 2.48167402E-09-1.03570916E-12 4.21059722E+04 1.84834973E+00 4.31525130E+04 4
NO RUS 89N 1O 1 0 0G 200.000 6000.000 1000. 1
 3.26071234E+00 1.19101135E-03-4.29122646E-07 6.94481463E-11-4.03295681E-15 2
 9.92143132E+03 6.36900518E+00 4.21859896E+00-4.63988124E-03 1.10443049E-05 3
-9.34055507E-09 2.80554874E-12 9.84509964E+03 2.28061001E+00 1.09770882E+04 4
N2O4 O2NNO2 ATcT AN 2.O 4. 0. 0.G 200.000 6000.000 1000. 1
 1.15752932E+01 4.01615532E-03-1.57178022E-06 2.68273657E-10-1.66921538E-14 2
-2.96111235E+03-3.19488625E+01 3.02002271E+00 2.95904359E-02-3.01342572E-05 3
 1.42360526E-08-2.44100411E-12-6.79238803E+02 1.18059620E+01 1.29712996E+03 4
NO2 T10/11N 1.O 2. 0. 0.G 200.000 6000.000 1000. 1
```

```
 5.45920936E+00 1.55554384E-03-6.04009241E-07 1.02552143E-10-6.35419893E-15 2
 4.03692954E+04-2.74941490E+00 3.16383599E+00 5.03834062E-03 3.57719973E-06 3
-1.01782549E-08 4.90582048E-12 4.11173009E+04 9.73195334E+00 4.22983435E+04 4
OH A 2Sigma+ ATcT AO 1.H 1. 0. 0.G 200.000 6000.000 1000. 1
 2.75582920E+00 1.39848756E-03-4.19428493E-07 6.33453282E-11-3.56042218E-15 2
 5.09751756E+04 5.62581429E+00 3.46084428E+00 5.01872172E-04-2.00254474E-06 3
 3.18901984E-09-1.35451838E-12 5.07349466E+04 1.73976415E+00 5.17770741E+04 4
O singlet (excite)ATcT AO 1. 0. 0. 0.G 200.000 6000.000 1000. 1
 2.49368475E+00 1.37617903E-05-1.00401058E-08 2.76012182E-12-2.01597513E-16 2
 5.19986304E+04 4.65050950E+00 2.49993786E+00 1.71935346E-07-3.45215267E-10 3
 3.71342028E-13-1.70964494E-16 5.19965317E+04 4.61684555E+00 5.27418934E+04 4
END
REACTIONS
!-----------------------------------------------------------------------
!Reactions    A n Ea
!-----------------------------------------------------------------------
N2O4 + M => NO2 + NO2 + M  1.960E+28 -3.800 12840.00
CH6N2 + NO2 => CH5N2 + HONO  2.200E+11 0.000 6700.00
CH5N2 + NO2 => CH4N2 + HONO  1.000E+08 2.000 0.00
CH4N2 + NO2 => CH3N2 + HONO  2.200E+11 0.000 6700.00
CH6N2 => CH4N2 + H2   3.260E+13 0.000 18700.00
HONO + M => NO + OH + M   8.400E+12 0.000 17000.00
NO2 => NO + O    0.760E+19 -1.270 73290.00
NO2 + H => NO + OH   0.350E+15 0.000 1500.00
CH3N2 => CH3 + N2   3.000E+06 0.000 0.00
H2 + OH => H2O + H   2.160E+10 1.510 0.00
CH3 + O => H + CH2O   8.430E+13 0.000 0.00
CH2O + O => OH + HCO   3.900E+13 0.000 3540.00
HCO + O => H + CO2   3.000E+13 0.000 0.00
CH3 + NO => HCN + H2O   9.600E+13 0.000 28800.00
HCN + M => H + CN + M   1.040E+29 -3.300 126600.00
CN + H2 => HCN + H   2.100E+13 0.000 4710.00
NH2 + H => NH + H2   4.000E+13 0.000 3650.00
NH + NO => N2 + OH   2.160E+13 -0.230 0.00
H2 + O => H + OH   5.060E+04 2.670 6290.63
HCN + OH => NH2 + CO   1.600E+02 2.560 9000.00
END
```

REFERENCES

[1] G. Dettleff, “Plume flow and plume impingement in space technology,” *Progress in Aerospace Sciences*, vol. 28, no. 1, pp. 1–71, Jan. 18, 1991.

[2] H. Trinks, “Experimental investigation of the exhaust plume flow fields of various small bipropellant and monopropellant thrusters,” in *AIAA-87-1607*, Honolulu, HI: AIAA, Jun. 8, 1987, p. 11. DOI: `10.2514/6.1987-1607`.

[3] M. Larin, F. Lumpkin Iii, and P. Stuart, “Modeling unburned propellant droplet distribution and velocities in plumes of small bipropellant thrusters,” in *35th AIAA Thermophysics Conference*, Anaheim,CA,U.S.A.: American Institute of Aeronautics and Astronautics, Jun. 11, 2001. DOI: `10.2514/6.2001-2816`. [Online]. Available: `https://arc.aiaa.org/doi/10.2514/6.2001-2816`.

[4] C. Soares, H. Barsamian, and S. Rauer, “Thruster plume induced contamination measurements from the PIC and SPIFEX flight experiments,” in *Optical System Contamination: Effects, Measurements, and Control VII*, SPIE, vol. 4774, 2002, pp. 199–209.

[5] C. Soares, R. Olsen, C. Steagall, *et al.*, “IMPROVEMENTS IN MODELING THRUSTER PLUME EROSION DAMAGE TO SPACECRAFT SURFACES,” in *International Symposium on Materials in the Space*, Jun. 2015.

[6] D. Coyle and L. Hampton, “21st century progress in computing,” *Telecommunications Policy*, vol. 48, no. 1, p. 102 649, 2024.

[7] M. Ivanov, G. Markelov, Y. I. Gerasimov, A. Krylov, L. Mishina, and E. Sokolov, “Free-flight experiment and numerical simulation for cold thruster plume,” *Journal of propulsion and power*, vol. 15, no. 3, pp. 417–423, 1998.

[8] F. Lumpkin III and M. Larin, “Simulation of the plume from the firing of four r4d engines on the h-2 transfer vehicle using the GASP and DAC codes,” in *29th JANNAF Exhaust Plume Technology Subcommittee Meeting, Littleton, CO*, 2006.

[9] K. H. Lee, “Comparison study of exhaust plume impingement effects of small mono- and bipropellant thrusters using parallelized DSMC method,” *PLOS ONE*, vol. 12, no. 6, X.-D. Wang, Ed., e0179351, Jun. 21, 2017, ISSN: 1932-6203. DOI: `10.1371/journal.pone.0179351`. [Online]. Available: `https://dx.plos.org/10.1371/journal.pone.0179351`.

[10] K. H. Lee, “Plume influence analysis of small bipropellant thruster on solar array of GEO satellite,” *PLOS ONE*, vol. 13, no. 9, M. Peters, Ed., e0199667, Sep. 4, 2018, ISSN: 1932-6203. DOI: `10.1371/journal.pone.0199667`. [Online]. Available: `https://dx.plos.org/10.1371/journal.pone.0199667`.

[11] L. Hou, P. Fu, and Y. Ba, “Chemical mechanism of MMH/NTO and simulation in a small liquid rocket engine,” *Combustion Science and Technology*, Nov. 2018.

[12] J. D. Anderson, *Hypersonic and High Temperature Gas Dynamics*, 3rd. AIAA, 1989.

[13] D. C. Wilcox *et al.*, *Turbulence Modeling for CFD*. DCW industries La Canada, CA, 1998, vol. 2.

[14] F. Menter, “Two-equation eddy-viscosity turbulence models for engineering applications,” *AIAA Journal*, vol. 32, no. 8, Aug. 1994.

[15] E. Loth, J. Tyler Daspit, M. Jeong, T. Nagata, and T. Nonomura, “Supersonic and hypersonic drag coefficients for a sphere,” *AIAA Journal*, vol. 59, no. 8, pp. 3261–3274, 2021.

[16] “The chemkin thermodynamic data base,” Sandia Report 87-8215B, Mar. 1990.

[17] A. N. Laboratories, *Ideal gas and condensed gas phase database for combustion*.

[18] N. I. of Standards and Technology, *NIST-JANAF tables of nitrogen*, version Fourth, 1998.

[19] P. Linstrom, *NIST chemistry WebBook - SRD 69*, 2017. DOI: `https://doi.org/10.18434/T4D303`.

[20] A. Rocketdyne, *In-space propulsion data sheets*, 2020.